A LES/PDF simulator on block-structured meshes

Hasret Turkeri, Stephen B. Pope & Metin Muradoglu

Published online: 22 Jun 2018.

Submit your article to this journal

Article views: 81

View Crossmark data

Taylor & Francis
Taylor & Francis Group

Check for updates

A LES/PDF simulator on block-structured meshes

Hasret Turkeri[a,b*], Stephen B. Pope[c] and Metin Muradoglu[a]

[a]Department of Mechanical Engineering, Koç University, Sariyer, Istanbul, Turkey; [b]Department of Mechanical Engineering, University of Connecticut, Storrs, CT, USA; [c]Sibley School of Mechanical and Aerospace Engineering, Cornell University, Ithaca, NY, USA

A block-structured mesh large-eddy simulation (LES)/probability density function (PDF) simulator is developed within the OpenFOAM framework for computational modelling of complex turbulent reacting flows. The LES/PDF solver is a hybrid solution methodology consisting of (i) a finite-volume (FV) method for solving the filtered mass and momentum equations (LES solver), and (ii) a Lagrangian particle-based Monte Carlo algorithm (PDF solver) for solving the modelled transport equation of the filtered joint PDF of compositions. Both the LES and the PDF methods are developed and combined to form a hybrid LES/PDF simulator entirely within the OpenFOAM framework. The *in situ* adaptive tabulation method [S.B. Pope, *Computationally efficient implementation of combustion chemistry using in situ adaptive tabulation*, Combust. Theory Model. 1 (1997), pp. 41–63; L. Lu, S.R. Lantz, Z. Ren, and B.S. Pope, *Computationally efficient implementation of combustion chemistry in parallel PDF calculations*, J. Comput. Phys. 228 (2009), pp. 5490–5525] is incorporated into the new LES/PDF solver for efficient computations of combustion chemistry with detailed reaction kinetics. The method is designed to utilise a block-structured mesh and can readily be extended to unstructured grids. The three-stage velocity interpolation method of Zhang and Haworth [*A general mass consistency algorithm for hybrid particle/finite-volume PDF methods*, J. Comput. Phys. 194 (2004), pp. 156–193] is adapted to interpolate the LES velocity field onto particle locations accurately and to enforce the consistency between LES and PDF fields at the numerical solution level. The hybrid algorithm is fully parallelised using the conventional domain decomposition approach. A detailed examination of the effects of each stage and the overall performance of the velocity interpolation algorithm is performed. Accurate coupling of the LES and PDF solvers is demonstrated using the one-way coupling methodology. Then the fully two-way coupled LES/PDF solver is successfully applied to simulate the Sandia Flame-D, and a turbulent non-swirling premixed flame and a turbulent swirling stratified flame from the Cambridge turbulent stratified flame series [M.S. Sweeney, S. Hochgreb, M.J. Dunn, and R.S. Barlow, *The structure of turbulent stratified and premixed methane/air flames I: Non-swirling flows*, Combust. Flame 159 (2012), pp. 2896–2911; M.S. Sweeney, S. Hochgreb, M.J. Dunn, and R.S. Barlow, *The structure of turbulent stratified and premixed methane/air flames II: Swirling flows*, Combust. Flame 159 (2012), pp. 2912–2929]. It is found that the LES/PDF method is very robust and the results are in good agreement with the experimental data for both flames.

Keywords: large-eddy simulation/probability density function; turbulent reacting flows; block structured meshes; OpenFOAM; Sandia flame-D; Cambridge stratified flame; velocity correction; turbulent premixed flame; turbulent non-premixed flame

---

*Corresponding author. Email: hturkeri@ku.edu.tr, hasretturkeri@gmail.com

1. Introduction

More than 85% of the total energy production in the world still comes from burning fossil fuels, i.e. converting chemical energy stored in hydrocarbon fuels first into thermal energy and then into mechanical energy in energy conversion devices, e.g. gas turbines and reciprocating engines, and fossil-fuel power stations [1]. In nearly all practical energy conversion devices combustion takes place in a turbulent environment mainly due to enhanced mixing [2]. Therefore accurate prediction of the properties of the turbulent reacting flows is crucial for increasing the efficiency of the combustion devices, and decreasing the dangerous effects of combustion on the environment, e.g. formation of NO_x, soot and unburnt hydrocarbons (HC), in addition to CO_2 that contributes to global warming.

The large-eddy simulation/probability density function (LES/PDF) method has been found to be highly effective in the simulation of turbulent reacting flows [3–7]. The main advantage of the PDF method for turbulent reacting flows is that arbitrarily complex non-linear chemical reactions and other one-point processes such as radiative heat transfer are treated exactly without any modelling assumption. Although LES has been very successful in modelling non-reacting turbulent flows, it suffers from the same closure problem for the reacting flows as do the Reynolds averaged Navier-Stokes (RANS) models since chemical reactions occur essentially at the smallest turbulent scales that need to be modelled in LES as in RANS [8]. Thus the LES/PDF method attempts to combine the best features of the LES and PDF methods and to avoid their deficiencies when used alone [9]. In this approach, the modelled filtered mass and momentum equations are solved together with the modelled transport equation for the joint-PDF of chemical compositions.

Application of the LES/PDF method to complex reacting flows of practical interest requires the development of an efficient and accurate numerical solution algorithm. The main difficulty arises from the solution of the joint-PDF transport equation that evolves in a high dimensional space and thus cannot be solved efficiently using the conventional numerical methods such as finite-volume and finite-element techniques. Of the remaining alternatives, the Monte Carlo method has proven to be suitable for solving high dimensional problems. In particular, the Lagrangian particle-based Monte Carlo methods have been demonstrated to be a viable tool for solving the joint-PDF transport equation [10]. Integration of the Lagrangian particle-based algorithms into existing Eulerian grid-based solvers is not easy but highly desirable for applications of the PDF methods to complex turbulent reacting flows in practical combustion devices. This has been one of the main motivations for the development of the hybrid finite-volume/particle solvers [11–13]. The hybrid methods were first developed for solving the RANS/PDF model equations [12,13] but they have been more recently shown also to be suitable for solving the LES/PDF model equations [14,15]. The hybrid method combines an Eulerian finite-volume (or difference) method for the filtered mass and momentum equations (referred as the LES solver) with a Lagrangian particle-based Monte Carlo algorithm (referred as the PDF solver). The hybrid LES/PDF solver provides a complete numerical solution method for the LES/PDF model equations of the turbulent reacting flows.

In the literature various hybrid LES/PDF solvers have been developed and successfully used for simulations of turbulent reacting flows. However, they have been mostly applied to laboratory scale turbulent flames with simple geometries [4,9,15–17]. The main reason is that the existing LES/PDF algorithms are mostly designed to work only on structured Eulerian grids. To the best of our knowledge, the only exceptions are the unstructured hybrid solvers developed by Ansari et al. [18] and Gupta [19]. Ansari et al. [18] constructed a

hybrid solver within a commercial platform of ANSYS-FLUENT software, which hinders its widespread use. Gupta [19] combined the LES solver in OpenFOAM [20] with an existing PDF solver written in FORTRAN. Although it has been successfully used in simulating various turbulent flames [19], the main drawback of this hybrid solver is the different data structures used in OpenFOAM and the PDF solver, which adversely affects computational efficiency. Therefore it is highly desirable to develop a hybrid method fully within the OpenFOAM framework.

In the present study, a new LES/PDF solver is developed entirely within the Open-FOAM framework. The open-source and free OpenFOAM framework [20] is preferred since it uses a field operation approach and thus provides a highly convenient platform for solving partial differential equations. OpenFOAM is widely used in both industry and academia, and includes a wide range of physical submodels. The new OpenFOAM-based hybrid LES/PDF solver uses block-structured grids and can readily be extended to unstructured grids, and thus allows LES/PDF simulations in complex geometries of practical interest. The method is designed to employ the most advanced physical submodels and numerical methods available in the literature. In particular, the *in situ* adaptive tabulation (ISAT) method [21,22] is incorporated into the new hybrid solver to perform detailed chemistry simulations efficiently. The PDF and LES solvers are both built within Open-FOAM libraries, thus the same data structure can be used in both solvers, which make the data transfer between them very efficient and flexible.

The hybrid LES/PDF method is fully consistent at the level of the model equations solved by the LES and PDF algorithms. However, inconsistencies may arise due to the accumulation of numerical errors. In the LES/PDF context, accurate interpolation of filtered velocity field from the Eulerian grid onto Lagrangian particles is crucially important to maintain consistency between the particle mass and LES density fields. It is a challenging problem to construct an interpolation scheme that satisfies the mass conservation at the discrete level [11,13]. In the present OpenFOAM-based LES/PDF solver, the three-stage velocity interpolation and correction algorithm of Zhang and Haworth [11] are adapted to the block-structured grid and shown to perform well. The velocity interpolation and correction algorithm was initially developed for unsteady and steady RANS/PDF simulations, and then extended to the LES/PDF methods [23] but it has not been fully tested for the LES/PDF simulations of complex turbulent flames. Celis and Silva [23] investigated the performance of the three-stage velocity correction method in the LES/PDF context but they considered only a simple mixing layer flow and performed simulations only on a simple structured uniform Cartesian grid. Thus, the present work is the first assessment of the performance of the method within the LES/PDF context using a complex block-structured grid for the realistic turbulent flames. The effects of each stage of the velocity interpolation and correction method on mass consistency, accuracy and computational cost are examined. It is shown that the method is very effective in enforcing the mass consistency in the present LES/PDF solver.

In this paper, the main contributions can be summarised as follows:

(1) The development and validation of a new LES/PDF method entirely within the OpenFOAM framework.
(2) The implementation and performance assessment of the three-stage velocity interpolation and correction algorithm on block-structured grid.
(3) An examination of the consistency between the LES and PDF solvers using the one-way coupling methodology.

(4) An investigation of the predictive capability of the fully two-way coupled LES/PDF solver with detailed chemistry representation for a piloted jet flame (Flame-D) and bluff-body stabilised turbulent non-swirling premixed and swirling stratified flames (Cambridge stratified flames).

The rest of the paper is organised as follows. In the next section, the governing equations of the LES/PDF method and the hybrid solution methodology are presented. In Section 3, the numerical methods used to solve the model equations of the LES/PDF method are described. In Section 4.1, the hybrid LES/PDF solver is applied to a methane/air jet diffusion flame and the performance of the new solver is demonstrated. In Section 5, the method is applied to turbulent non-swirling premixed and swirling stratified flames from the Cambridge stratified turbulent flame series [24]. The conclusions and future directions are presented in Section 6.

2. LES/PDF method

2.1. *Governing equations*

In the LES method, the fields in a turbulent reacting flow are separated into large (filtered or resolved) and small (unresolved) scales by applying a low-pass filtering operation. For example, the filtered (resolved) density field $\bar{\rho}$ is defined as

$$\bar{\rho} \equiv \int_{-\infty}^{\infty} \rho(\mathbf{y}, t) G(\mathbf{y} - \mathbf{x}) \, d\mathbf{y}, \tag{1}$$

where $\rho(\mathbf{x}, t)$ is density field and G is the LES filter. Applying this filter to the instantaneous mass and momentum conservation equations, one can obtain

$$\frac{\partial \bar{\rho}}{\partial t} + \frac{\partial \bar{\rho} \tilde{u}_i}{\partial x_i} = 0, \tag{2}$$

$$\frac{\partial \bar{\rho} \tilde{u}_i}{\partial t} + \frac{\partial \bar{\rho} \tilde{u}_i \tilde{u}_j}{\partial x_j} = -\frac{\partial \bar{p}}{\partial x_i} + \frac{\partial \tau_{ij}}{\partial x_j} + \frac{\partial T_{ij}}{\partial x_j}, \tag{3}$$

where $\tilde{u}_i$ and $\bar{p}$ are the Favre-filtered velocity and the filtered pressure fields, respectively. In Equation (3), the resolved viscous stress tensor is approximated as

$$\tau_{ij} = \tilde{\mu} \left(\frac{\partial \tilde{u}_i}{\partial x_j} + \frac{\partial \tilde{u}_j}{\partial x_i} - \frac{2}{3} \frac{\partial \tilde{u}_k}{\partial x_k} \delta_{ij} \right), \tag{4}$$

where $\tilde{\mu}$ is resolved molecular viscosity. The last term on the right-hand side of Equation (3) represents the unclosed subfilter stress tensor defined as $T_{ij} = \bar{\rho} \tilde{u}_i \tilde{u}_j - \bar{\rho} \widetilde{u_i u_j}$, and it is modelled using the dynamic Smagorinsky model of Moin et al. [25] with the Lagrangian averaging method developed by Meneveau et al. [26].

For a variable-density flow, the filtered mass density function (FMDF) [3,9] is defined as

$$\mathcal{F}(\boldsymbol{\psi}; \mathbf{x}, t) \equiv \int_{-\infty}^{\infty} \rho(\mathbf{y}, t) \delta(\boldsymbol{\psi} - \boldsymbol{\phi}(\mathbf{y}, t)) G(\mathbf{y} - \mathbf{x}) \, d\mathbf{y}, \tag{5}$$

where $\boldsymbol{\phi}$ represents the $N = N_s + 1$ compositional scalars consisting of the mass fractions of N_s species and sensible enthalpy, $\boldsymbol{\psi}$ is the sample space variable for the compositions

and δ is the N-dimensional delta function. The Favre-filtered PDF $\tilde{f}$ is related to the FMDF as $\tilde{f} = \mathcal{F}/\bar{\rho}$. The Favre-filtered mean of any flow variable Q known in terms of $\boldsymbol{\phi}$ can be defined as

$$\tilde{Q}(\boldsymbol{x}, t) = \frac{1}{\bar{\rho}} \int Q(\boldsymbol{\psi}; \boldsymbol{x}, t) \mathcal{F}(\boldsymbol{\psi}; \boldsymbol{x}, t) \, \mathrm{d}\boldsymbol{\psi} = \int Q(\boldsymbol{\psi}; \boldsymbol{x}, t) \tilde{f}(\boldsymbol{\psi}; \boldsymbol{x}, t) \, \mathrm{d}\boldsymbol{\psi}. \tag{6}$$

In particular, the filtered density field can be recovered by integrating the FMDF over the entire sample space, i.e.

$$\bar{\rho}(\boldsymbol{x}, t) = \int \mathcal{F}(\boldsymbol{\psi}; \boldsymbol{x}, t) \, \mathrm{d}\boldsymbol{\psi}. \tag{7}$$

The conservation equation for composition ϕ_α can be written as

$$\frac{\partial \rho \phi_\alpha}{\partial t} + \frac{\partial \rho u_i \phi_\alpha}{\partial x_i} = -\frac{\partial J_i^\alpha}{\partial x_i} + S_\alpha, \tag{8}$$

where S_α represents the source term due to chemical reactions and J_i^α is the molecular diffusion term approximated as

$$J_i^\alpha = -\rho D_{(\alpha)} \frac{\partial \phi_\alpha}{\partial x_i} + \rho \phi_\alpha \boldsymbol{V}_c, \tag{9}$$

where $D_{(\alpha)}$ is the molecular diffusivity of species α computed using the CHEMKIN's TRANLIB subroutine. $\boldsymbol{V}_c = \sum_{\beta=1}^{Ns} D_{(\beta)} (\partial \phi_\beta / \partial x_i)$ is a correction velocity where N_s is number of species. The exact transport equation for the Favre-filtered PDF $\tilde{f}$ can be derived from Equations (5) and (8), and is given by [3,9]

$$\frac{\partial \bar{\rho} \tilde{f}}{\partial t} + \frac{\partial \bar{\rho} \tilde{u}_i \tilde{f}}{\partial x_i} + \frac{\partial \bar{\rho} \left(\widetilde{u_i'' \mid \boldsymbol{\psi}} \right) \tilde{f}}{\partial x_i}$$

$$= \frac{\partial}{\partial \psi_\alpha} \left[\tilde{f} \left(\overline{\frac{\partial}{\partial x_i} \left[\rho D_{(\alpha)} \frac{\partial \phi_\alpha}{\partial x_i} - \rho \phi_\alpha \boldsymbol{V}_c \right] \middle| \boldsymbol{\psi}} \right) \right] + \frac{\partial}{\partial \psi_\alpha} \left[\bar{\rho} \tilde{f} S_\alpha(\boldsymbol{\psi}) \right]. \tag{10}$$

The last term in Equation (10) represents the change of $\tilde{f}$ in the compositions space due to chemical reactions, and it appears in the closed form. The first two terms on the left-hand side represent the rate of change following the filtered (resolved) flow. The last term on the left-hand side represents the transport of $\tilde{f}$ in the physical space due to the small-scale (unresolved) velocity field $\boldsymbol{u}'' = \boldsymbol{u} - \tilde{\boldsymbol{u}}$ where $\widetilde{u_i'' \mid \boldsymbol{\psi}}$ is the mean of unresolved velocity conditional upon the event $\boldsymbol{\phi} = \boldsymbol{\psi}$ and is unclosed. This term is usually modelled by the gradient diffusion assumption as

$$\left(\widetilde{u_i'' \mid \boldsymbol{\psi}} \right) \tilde{f} = -\tilde{D}_T \frac{\partial \tilde{f}}{\partial x_i}. \tag{11}$$

Here, $\tilde{D}_T$ is the turbulent diffusivity and it is obtained from the turbulent eddy viscosity as $\bar{\rho} \tilde{D}_T = \tilde{\mu}_T / Sc_T$ where Sc_T is the turbulent Schmidt number with the constant value of

$Sc_T = 0.4$ [27]. The first term on the right-hand side of Equation (10) represents the change of $\tilde{f}$ in the compositions space due to the molecular mixing and is modelled as [28]

$$\frac{1}{\bar{\rho}} \overline{\frac{\partial}{\partial x_i}\left(\rho D_{(\alpha)}\frac{\partial \phi_\alpha}{\partial x_i}\right)\Bigg|\,\psi} = -\Omega\left(\psi_\alpha - \tilde{\phi}_\alpha\right) + \frac{1}{\bar{\rho}}\frac{\partial}{\partial x_i}\left(\bar{\rho}\tilde{D}_{(\alpha)}\frac{\partial \tilde{\phi}_\alpha}{\partial x_i} - \bar{\rho}\tilde{\phi}_\alpha \boldsymbol{V}_c\right), \quad (12)$$

where the first term on the right-hand side represents the interaction by exchange with the mean (IEM) mixing model [29] and the second term is the mean drift term [28]. In Equation (12), Ω denotes the scalar mixing frequency and it can be modelled as

$$\Omega = C_m \frac{\tilde{D} + \tilde{D}_T}{\Delta^2}, \quad (13)$$

where C_m is a model constant determined by the sensitivity study on the statistics obtained by the simulations, $\tilde{D}$ is the thermal diffusivity, and Δ is the LES filter size.

2.2. *Solution methodology for the LES/PDF model equations*

The filtered conservation of mass and momentum equations (Equations (2) and (3)) can be solved numerically by conventional methods such as finite volume or finite difference techniques. However, the conventional methods are not feasible for solving the filtered joint-PDF transport equation due to its high dimensionality. Pope proposed [10] an alternative solution methodology for the joint-PDF transport equation based on the Monte Carlo method in the Lagrangian frame. In this approach, the flow is represented by a large number of notional Lagrangian particles. Then a set of stochastic differential equations are constructed to evolve particle properties such that the particles exhibit the same joint PDF as the one obtained from the solution of the modelled joint-PDF transport equation. In this approach, the particle position and compositions evolve by Pitsch and Steiner [28]

$$dX_j^* = \left[\tilde{u}_j + \frac{1}{\bar{\rho}}\frac{\partial(\bar{\rho}\tilde{D}_T)}{\partial x_j}\right]^* dt + \left[2\tilde{D}_T^*\right]^{1/2} dW_j^*, \quad (14)$$

$$d\phi_\alpha^* = -\Omega^*(\phi_\alpha^* - \tilde{\phi}_\alpha^*)\,dt + \left[\frac{1}{\bar{\rho}}\frac{\partial}{\partial x_j}\left(\bar{\rho}\tilde{D}_{(\alpha)}\frac{\partial \tilde{\phi}_\alpha}{\partial x_j} - \bar{\rho}\tilde{\phi}_\alpha \boldsymbol{V}_c\right)\right]^* dt + S_\alpha(\boldsymbol{\phi}^*)\,dt, \quad (15)$$

where $d\boldsymbol{W}^*$ denotes the Wiener increment. Equation (14) evolves the particle properties in physical space while Equation (15) evolves the particle properties in the composition space. The superscript '*' denotes the particle properties, or the LES fields evaluated at the particle locations.

The resulting solution methodology is composed of two main components: (i) An Eulerian finite-volume method for solving the filtered conservation equations for the mass and momentum (the LES solver). (ii) A Lagrangian Monte Carlo method for the transport equation for the joint PDF of compositions (the PDF solver). The LES and PDF solvers together form the hybrid LES/PDF solver to be used for simulating turbulent reacting flows. In the hybrid LES/PDF method, the LES solver calculates the velocity, $\tilde{u}_i$, the turbulent viscosity $\tilde{\mu}_T$ and diffusivity $\tilde{D}_T$ as well as the mixing frequency Ω. The PDF solver evolves the particle properties in the physical and compositions spaces and calculates the filtered density $\bar{\rho}$, the Favre-filtered temperature $\tilde{T}$ and mass fractions $\tilde{Y}_\alpha$.

In the LES solver, the filtered density, $\bar{\rho}$, is required to solve Equations (2) and (3). On the other hand, the PDF solver requires the fields of Favre-filtered velocity, $\tilde{u}_i$, the turbulent diffusivity, $\tilde{D}_T$, and the mixing frequency Ω in the particle equations, i.e. Equations (14) and (15). Therefore, the LES supplies the Favre-filtered velocity, $\tilde{u}_i$, the turbulent diffusivity, $\tilde{D}_T$ and the mixing frequency, Ω, fields to the PDF solver in each time step. In turn, the LES solver receives the filtered density $\bar{\rho}$ and the Favre-filtered temperature $\tilde{T}$ from the PDF solver.

While the data transfer from the LES solver to the PDF solver is usually done by directly interpolating the LES fields onto particle locations, the filtered density feedback from the PDF solver to the LES solver is a challenging task due to the stochastic nature of the particle fields. The mean fields extracted from particles contain significant stochastic noise, thus using the noisy particle density field directly in the LES solver is prone to cause a significant numerical instability problem. We note that the numerical instability is mainly caused by the term containing time derivative of the filtered density in the pressure equation.

To overcome this difficulty, we employ the transported specific volume (TSV) method developed by Popov et al. [30]. In the TSV method, the change in the resolved specific volume due to transport in the physical space (Equation (14)) is calculated by the LES solver and the changes due to turbulent mixing, molecular diffusion and chemical reactions (the terms on the right-hand side of Equation (15), respectively) are calculated by the PDF solver. For this purpose, the evolution equation for the specific volume, $\tilde{v}$, is derived from the modelled FMDF equation and augmented by a relaxation term. The resulting equation can be written as

$$\frac{\partial \bar{\rho}\tilde{v}}{\partial t} + \frac{\partial \left(\bar{\rho}\tilde{u}_j\tilde{v}\right)}{\partial x_j} = \frac{\partial}{\partial x_j}\left(\bar{\rho}\tilde{D}_T\frac{\partial \tilde{v}}{\partial x_j}\right) + S_v + \dot{\omega}_v, \tag{16}$$

where S_v is the source term defined as

$$S_v \equiv \left\{\frac{\sum \dot{v}^*}{\sum v^*}\right\}, \tag{17}$$

where $\sum \dot{v}^*$ is the mass weighted sum of the rate of change of particle specific volume in a given cell due to mixing, molecular diffusion and chemical reaction, while $\sum v^*$ is the mass weighted sum of particle specific volume in the same cell. The last term on the right-hand side of Equation (16) is the relaxation term of the form

$$\dot{\omega}_v = \bar{\rho}\frac{\tilde{v}_{PDF} - \tilde{v}}{\tau_v}, \tag{18}$$

where $\tilde{v}_{PDF}$ is the specific volume obtained from the particles in the PDF method and τ_v is the relaxation time scale taken here as $\tau_v = 4\Delta t$ with Δt being the time step. Once the specific volume is computed from Equation (16), the filtered density field $\bar{\rho}$ is obtained as

$$\bar{\rho} = \frac{1}{\tilde{v}}. \tag{19}$$

3. Numerical method

3.1. *LES solver*

The LES equations (Equations (2), (3) and (16)) are solved in OpenFOAM using a finite-volume method on a block-structured mesh with a collocated arrangement. Second-order

central differences are used to approximate all spatial derivatives except for the convective terms in the scalar equation (Equation (16)), which is discretised using the SuperBee flux limiter [31] to avoid unphysical excessive oscillations. Time integration is performed using a second-order backward differentiation scheme for all the LES equations. The flow and scalar equations are solved sequentially (i.e. segregated from each other). The iterations within each time step are called outer iterations and are repeated until the error is reduced below a prescribed error tolerance. In each outer iteration the pressure-velocity coupling is achieved using the PISO [32] method in which the velocity is corrected by solving a pressure Poisson equation iteratively. The iterations in solving the Poisson equation are called the inner iterations. In this study, the variable-density low-Mach number LES solver is developed by modifying the *pimpleFoam* solver originally designed to solve constant density flows in OpenFOAM. To do that, the density and the time derivative of density fields are added to the momentum and pressure solvers, respectively [33]. Within the outer loop, first the transport equation for specific volume Equation (16) is solved and the density field is updated using Equation (19). Then the momentum and pressure equations are solved, respectively. The flow chart of the LES solver is given in Figure 1.

3.2.   *PDF solver*

The coupled particle equations, Equations (14) and (15), are solved using a fractional time stepping method in which a fractional time step is taken for each physical process: transport in physical space $\mathbb{T}$; mixing and molecular diffusion $\mathbb{M}$; and, reaction $\mathbb{R}$. The three physical processes of $\mathbb{T}$, $\mathbb{M}$ and $\mathbb{R}$ are represented by following equations:

$$\mathbb{T} : \mathrm{d}X_j^* = \left[\tilde{u}_j + \frac{1}{\bar{\rho}} \frac{\partial(\bar{\rho}\tilde{D}_T)}{\partial x_j} \right]^* \mathrm{d}t + \left[2\tilde{D}_T^* \right]^{1/2} \mathrm{d}W_j^*, \tag{20}$$

$$\mathbb{M} : \mathrm{d}\phi_\alpha^* = -\Omega^*(\phi_\alpha^* - \tilde{\phi}_\alpha^*)\, \mathrm{d}t + \left[\frac{1}{\bar{\rho}} \frac{\partial}{\partial x_j} \left(\bar{\rho}\tilde{D}_{(\alpha)} \frac{\partial \tilde{\phi}_\alpha}{\partial x_j} - \bar{\rho}\tilde{\phi}_\alpha \mathbf{V}_c \right) \right]^* \mathrm{d}t, \tag{21}$$

$$\mathbb{R} : \mathrm{d}\phi_\alpha^* = S_\alpha(\boldsymbol{\phi}^*)\, \mathrm{d}t. \tag{22}$$

We use the first-order fractional time stepping scheme ($\mathbb{TMR}$) to integrate the particle equations in time. We describe the method in detail below where the superscripts $(.)^n$ and $(.)^{n+1}$ denote the properties at time t_n and $t_n + \Delta t$, respectively.

(1) At the beginning of the particle time step, the particles are moved in the physical space for a full time step Δt according to Equation (20). The time integration is performed using the first-order Euler scheme [34] as

$$X_j^{*,n+1} = X_j^{*,n} + \left[\tilde{u}_j^n + \frac{1}{\bar{\rho}^n} \frac{\partial \bar{\rho}^n \tilde{D}_T^n}{\partial x_j} \right]^* \Delta t + \left(2\tilde{D}_T^n \Delta t \right)^{1/2} \eta_j^*, \tag{23}$$

where η_j^* is a standardised Gaussian random vector. To control the numerical error introduced by this simple first-order scheme, and maintain numerical stability, time step for each particle is restricted by the particle Courant number is defined as $CFL^* \equiv |\boldsymbol{u}^*|\Delta t^*/\mathcal{L}^e$ where $|\boldsymbol{u}^*|$ is the LES velocity at the particle location and $\mathcal{L}^e$ is a characteristic length of the *e*th computational cell. In this study, we set the particle
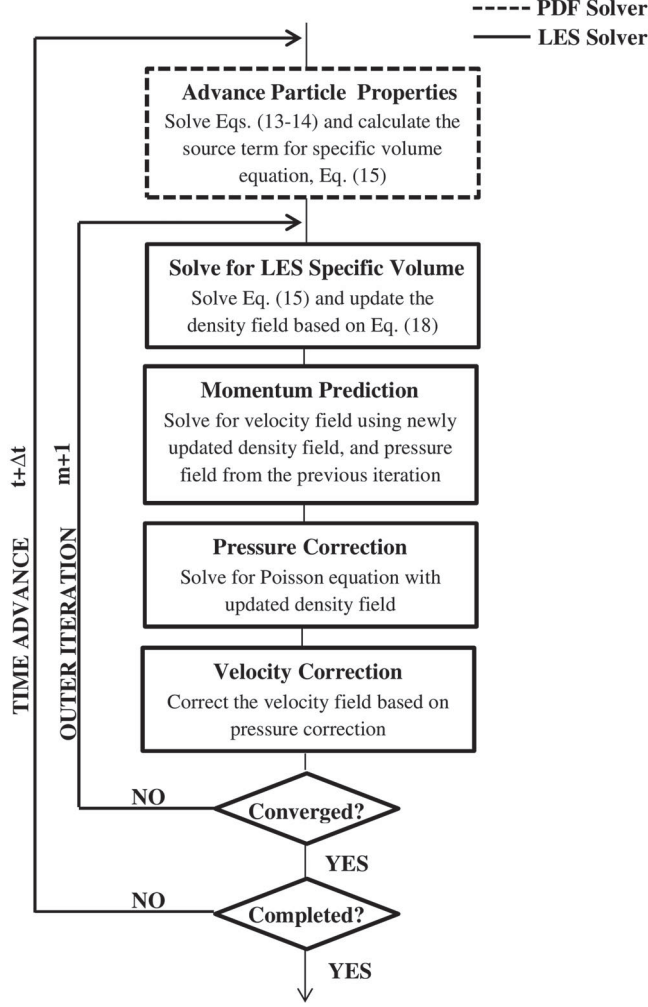
Figure 1. The flow chart of the LES/PDF solver.

Courant number to a fixed value of $CFL^* = 0.1$. This small value is used for the particle Courant number mainly to resolve the transient flow field accurately. The time step size is split into substeps when Δt^* is less than Δt.

(2) For the mixing and molecular transport steps, we follow the method developed by McDermott and Pope [28]. At the new particle position $X^{*,n+1}$, the particle composition is updated due to the mixing and molecular diffusion. Time integration of Equation (21) is achieved using a semi-analytical first-order scheme as

$$\phi_\alpha^{*,k} = \phi_\alpha^{*,n} + c^{*,n} \left(\tilde{\phi}_\alpha^{*,n} - \phi_\alpha^{*,n} \right) + \Delta \tilde{\phi}_\alpha^{*,n}, \tag{24}$$

where superscript $(.)^k$ denotes the intermediate step between the mixing and reaction, and $c^n = 1 - \exp(-\Omega^n \Delta t)$ is the decay factor calculated at cell centres and then interpolated onto particle locations. The term $\tilde{\phi}_\alpha^{*,n}$ is the mean composition that is first

estimated from the particle properties using a mass/decay-factor weighting and then interpolated on the particles. As shown by Jenny et al. [35] and McDermott and Pope [28], $\tilde{\phi}_\alpha^{*,n}$ must be evaluated using a mass/decay-factor weighting to satisfy the detailed conservation. $\Delta\tilde{\phi}_\alpha$ is the mean drift term calculated as

$$\Delta\tilde{\phi}_\alpha^n = \Delta\tilde{\phi}_\alpha^{FV} - \frac{1}{N_s}\sum_{\beta=1}^{N_s}\Delta\tilde{\phi}_\beta^{FV}, \qquad (25)$$

where N_s is number of species and $\Delta\tilde{\phi}_\alpha^{FV}$ is calculated using the finite-volume approach as

$$\Delta\tilde{\phi}_\alpha^{FV} = \left[\frac{1}{\bar{\rho}^n}\frac{\partial}{\partial x_j}\left(\bar{\rho}^n\tilde{D}_{(\alpha)}^n\frac{\partial\tilde{\phi}_\alpha^n}{\partial x_j}\right) - \frac{1}{\bar{\rho}^n}\frac{\partial}{\partial x_j}\left(\bar{\rho}^n\tilde{\phi}_\alpha^n V_c^n\right)\right]\Delta t. \qquad (26)$$

The second term on the right-hand side of Equation (25) is used to satisfy the realizability constraint which requires $\sum_{\alpha=1}^{N_s}\phi_\alpha = 1$ [28]. The mean drift term $\Delta\tilde{\phi}_\alpha^n$ is calculated at the cell centres and then interpolated onto the cell vertices and finally onto the particle locations. The interpolation of LES fields onto particle locations will be described in Section 3.2.3. The realizability constraint also demands the boundedness of species mass fractions, which requires that mass fractions be positive at all times, i.e. $\phi_\alpha \geq 0$. The boundedness constraint requires that at the jth cell centre c_j^n satisfies

$$c_j^n \geqslant c_j^{\min} \equiv \max_{k\in\mathcal{C}_N}\left(\left[\frac{\Delta\tilde{\phi}_{\alpha,k}}{\phi_{\alpha,\min}^n - \tilde{\phi}_{\alpha,k}^n}\right], \left[\frac{\Delta\tilde{\phi}_{\alpha,k}}{\phi_{\alpha,\max}^n - \tilde{\phi}_{\alpha,k}^n}\right]\right), \qquad (27)$$

where $\mathcal{C}_N$ is the set of cells sharing the vertices of the jth cell, $\phi_{\alpha,\min}^n$ and $\phi_{\alpha,\max}^n$ are the minimum and maximum values of particles within the cells in $\mathcal{C}_N$, respectively. Therefore, after calculating the mean drift term $\Delta\tilde{\phi}_\alpha^n$ according to Equation (25), c_j^n values are updated as $c_j^n = c_j^{\min}$ if c_j^n is less than $c_j^{\min}$, and then the mean composition $\tilde{\phi}_\alpha^{*,n}$ is calculated again using updated c^n to be used in Equation (24).

(3) Using the particle composition $\phi_\alpha^{*,k}$ as the initial condition, the reaction fractional step (Equation (22)) is performed using the ISAT [21,22] package to obtain the composition at the new time level $\phi_\alpha^{*,n+1}$.

The scheme described above is nominally first-order accurate in time. Although a second-order time integration algorithm can be readily incorporated into the present hybrid method, we use the first-order method since Wang and Pope [15] have reported that the first-order methods can perform as well as the second-order accurate methods for the turbulent jet diffusion flame.

3.2.1. *Parallel particle tracking algorithm*

The OpenFOAM's particle tracking libraries are used to track the Lagrangian particles in the PDF solver [36]. The algorithm is described here for a two-dimensional case for simplicity and extension to three-dimensional case is straightforward. Assume that a particle initially located at position A in a given cell (host cell) moves to a new position B as sketched in Figure 2. If point B is within the same cell as point A, then B is assigned as
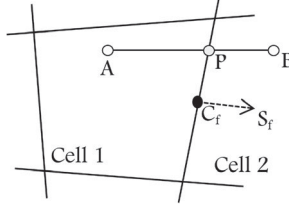
Figure 2. The schematic representation of the OpenFOAM particle tracking algorithm on an unstructured grid.

the new particle position at the new time step and this assignment completes the tracking for the current time step. However, if the particle intersects a face of the cell at a point P then it stops at P and changes its pointer for the neighbouring cell, and then continues its motion within the neighbouring cell until reaching the final destination of point B. The intersection point P can be computed as

$$P = A + \lambda_f (B - A), \tag{28}$$

where $\lambda_f = |AP|/|AB|$ is the fraction of the line segment and is calculated as

$$\lambda_f = \frac{(C_f - A) \cdot S_f}{(B - A) \cdot S_f}, \tag{29}$$

where C_f is the centre of the face and S_f is the face unit normal vector.

Particles are simply reflected from the physical boundaries back into the computational domain but a special treatment is needed in the case that a particle crosses an internal domain boundary. When a particle that is initially assigned to processor k moves and hits an inter-processor-face shared by processors k and l, then the particle is transferred from processor k–l using the MPI communication. The tracking algorithm can be summarised as follows:

(1) Label initially all the particles as 'active' and set the time to be tracked as $t_{track} = \Delta t$.
(2) For a given particle, calculate λ values for all the faces of the host cell.
(3) Find the minimum value $\lambda_{\min}$ in the interval $0 \le \lambda \le 1$, among all the λ_f values. The face associated with $\lambda_{\min}$ is to be crossed by the particle.
(4) If $\lambda_{\min}$ is equal to zero, the final destination is inside the host cell, so move the particle directly to point B and complete the tracking.
(5) If $\lambda_{\min}$ is greater than zero, first move the particle until the intersection point P and reduce the particle's tracking time t_{track}^k as

$$t_{track}^{k+1} = t_{track}^k - \lambda \Delta t, \tag{30}$$

where t_{track}^k denotes the remaining time for the particle to complete the time step.
(6) If the face crossed by the particle is an internal face (shared by two cells both in the same subdomain), then change the cell pointer of the particle to the neighbouring cell.
(7) If the face crossed by the particle is an inter-processor-face between the host processor k and a neighbouring processor l, then add the particle index into a particle

transfer list holding the indices of the particles to be transferred from the processor k–l, and label the particle as 'passive'.

(8) For all the 'active' particles, repeat the steps from (2) to (7) until t_{track}^k of all 'active' particles become zero.

(9) Transfer all the particles in the particle transfer lists between processors via a MPI communication.

(10) For all the particles having t_{track}^k greater than zero, repeat the steps from (1) to (9) until the particle transfer list becomes empty. This ensures that the tracking time for all the particles is reduced to zero.

3.2.2. *Estimation of particle mean fields*

Estimation of mean quantities from stochastic particles is an important issue in the LES/PDF method. The particle mean fields are needed to close the particle and LES equations, and also to represent the computational results. The cloud-in-cell (CIC) method of Zhang and Haworth [11] is adapted here to estimate the mean fields from the noisy particle properties. The method is closely related and essentially an extension of the CIC method developed by Dreeben and Pope [37] to the non-Cartesian grids. In this approach, the mean values are evaluated at the cell vertices. The mean at the jth vertex is obtained from the particles within the cells that share the jth vertex (a set of cells, $\mathcal{C}_j$). The mean at the jth vertex is estimated as

$$\tilde{\phi}_{(j)} = \frac{\sum_{k=1}^{N_p} \omega_k^* \phi_k^* b_{k,j}}{\sum_{k=1}^{N_p} \omega_k^* b_{k,j}}, \tag{31}$$

where N_p is total number of particles in $\mathcal{C}_j$, ω_k^* is the weight of the individual particle (e.g. its mass), and $b_{k,j}$ is the tri-linear basis function of the kth particle corresponding to the jth vertex. Here the tri-linear basis function $b_{k,j}$ is based on the logical coordinates ζ_i of the particles within the computational cell. The logical coordinate system ζ_i is formed by transforming the physical coordinate system x_i in each cell. We use the isoparametric transformation of Zhang and Haworth [11] to define the local coordinates (also called the logical coordinates). Within a computational cell, the physical coordinates x_i are transformed into the logical coordinates ζ_i as shown in Figure 3. As explained in [11], the logical coordinates of any point in a computational cell can be approximated using the heights of the point from the faces of the cell as

$$\zeta_1 = \frac{h_1}{h_1 + h_2}, \quad \zeta_2 = \frac{h_3}{h_3 + h_4}, \quad \zeta_3 = \frac{h_5}{h_5 + h_6}, \tag{32}$$

where h_i is the height of the point from the ith face of the cell as shown in Figure 3. Then the tri-linear basis functions for each vertex of the host cell can be written as

$$\begin{aligned}
b_1 &= (1 - \zeta_1)(1 - \zeta_2)(1 - \zeta_3), \quad b_2 = \zeta_1(1 - \zeta_2)(1 - \zeta_3), \\
b_3 &= \zeta_1\zeta_2(1 - \zeta_3), \quad b_4 = (1 - \zeta_1)\zeta_2(1 - \zeta_3), \\
b_5 &= (1 - \zeta_1)(1 - \zeta_2)\zeta_3, \quad b_6 = \zeta_1(1 - \zeta_2)\zeta_3, \\
b_7 &= \zeta_1\zeta_2\zeta_3, \quad b_8 = (1 - \zeta_1)\zeta_2\zeta_3.
\end{aligned} \tag{33}$$

We note that the basis functions are defined only for the vertices of the host cell, therefore for the other vertices outside of the host cell of a given particle, the basis functions are equal to zero.
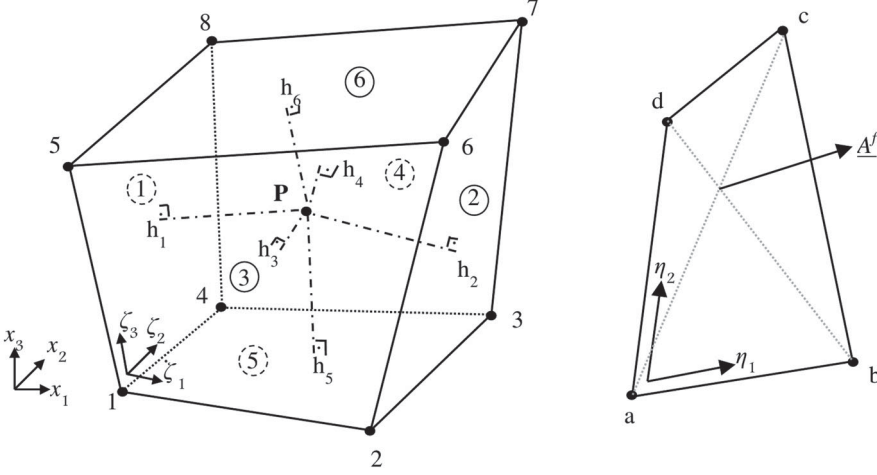
Figure 3. Isoparametric representation. The logical coordinates $(\zeta_1, \zeta_2, \zeta_3)$ (left). The logical coordinates (η_1, η_2) on a face of the cell (right).

3.2.3. *Interpolation of mean quantities onto particles*

The mean estimation method described in the previous section calculates the mean properties at the cell vertices. Some mean properties such as mean compositions are used in the particle equations, thus they need to be evaluated at the particle locations. Also, some particle means, e.g. the mean specific volume and the mean temperature are needed in the LES solver, thus they are required to be evaluated at the cell centres. Therefore, as needed, mean properties at the cell vertices are interpolated onto the Lagrangian particle locations and also onto the cell centres by using the tri-linear basis functions discussed in the previous section. The mean properties at the ith particle location are calculated as

$$\tilde{\phi}_i^* = \sum_{j=1}^{N_v} \tilde{\phi}_{(j)} b_{i,j}, \tag{34}$$

where N_v is the total number of vertices of the host cell, $\tilde{\phi}_{(j)}$ is the mean field at the jth vertex and $b_{i,j}$ is the basis function of ith particle corresponding to the jth vertex.

Several FV fields such as $\tilde{u}_i$, Ω, $\bar{\rho}$ and $\tilde{D}_T$ are also required at the Lagrangian particle positions to close the particle equations. Since the FV fields are located at the cell centres, they are first interpolated from the cell centres onto the cell vertices and then onto the particle locations using the tri-linear interpolations in the same way as in Equation (34).

3.2.4. *Three-stage velocity interpolation and correction method*

Accurate interpolation of the LES velocity field onto particle positions is crucially important to satisfy the consistency between the particle mass and LES density fields. The consistency condition in the hybrid LES/PDF method requires that the mean particle mass distribution in the PDF method should be consistent with the fluid mass distribution in the LES solver, and this consistency should be satisfied throughout the simulation. Although the hybrid method is fully consistent at the level of equations solved by the LES and PDF solvers, deviations between the particle mass and LES density fields arise due to

the accumulation of numerical errors. A correction algorithm is needed to control the spatial distribution of particles and thus enforce the consistency between the LES and particle fields. In this study, a three-stage velocity interpolation method developed by Zhang and Haworth [11] is employed to interpolate the velocity field onto particles and to enforce the consistency condition. The method is reviewed only briefly here since it has been described in detail in [11].

The method consists of three stages:

- Stage 1: The cell centred LES velocity fields are first interpolated onto the cell vertices. Then the velocities are interpolated from the cell vertices onto the particle locations using the tri-linear interpolation in Equation (34).
- Stage 2: The first correction velocity field U_c^{S2} is calculated to make the mass fluxes from the kth cell across the face f, $Q^{k,f,TL}$, implied by the tri-linear interpolation scheme consistent with the mass flux in the finite volume (LES) solver $Q^{k,f,FV}$. This requires determination of 24 correction velocity components (3 velocity components for each of the 8 element vertices) subject to 24 constraints. For this purpose, a system of 24 linear equations is solved to calculate the correction velocities for each cell.
- Stage 3: This stage aims to drive the deviation between the fluid mass in the LES solver m^{FV} and the particle mass in the PDF solver m^p to zero in each cell. For this purpose, the time-scaled deviation or the mass residual, R^k, is defined for the kth cell as

$$R^k \equiv \frac{m^{k,FV} - m^{k,p}}{\tau_{S3}}, \tag{35}$$

where τ_{S3} is a relaxation time scale defined as $\tau_{S3} = \alpha \Delta t$ with α being a constant to be specified. The main purpose of this stage is to calculate the element-face mass flow rates, $\hat{Q}^{k,f}$, that satisfy

$$R^k = -\sum_{f \in k} \hat{Q}^{k,f}. \tag{36}$$

Equation (36) is in the same form as the discretized pressure Poisson equation solved in the PISO scheme [32], so it can be solved by the same linear equation solver. Once the cell-face flow rates, $\hat{Q}^{k,f}$, are determined from Equation (36), a set of cell-level correction velocities, U_c^{S3}, are constructed using the same procedure as in Stage 2.

The three-stage velocity interpolation algorithm can be summarised as:

(1) Interpolate the LES velocities from the cell centres onto the cell vertices, referred to as U_c^{S1}.
(2) Calculate the Stage 2 correction velocity, U_c^{S2}, at the cell vertices.
(3) Using the combined velocity, $U_c^{S1} + U_c^{S2}$, move the particles in the physical space according to Equation (23).
(4) Calculate the particle mass residual, R^k, for each cell.
(5) Then, solve the linear system of equations (Equation (36)) for the Stage 3 velocity, U_c^{S3}.
(6) Interpolate U_c^{S3} onto particle locations and move the particles with U_c^{S3*} to enforce the mass consistency.

More details of the velocity correction method can be found in [11].

3.2.5. *Particle number density control*

A nominal number of particles are initially distributed uniformly at random in each grid cell such that the particle properties are consistent with the underlying finite-volume fields. A cloning and combination procedure is applied at every time step to keep number of particles in each cell nearly uniform. Various particle number density control procedures have been reviewed by Haworth [14] including the present method, so it is briefly described here for completeness. The number of particles in each cell is checked at the end of each global time step. Particle cloning or combination is carried out if the number of particles in a cell is less than a prescribed minimum or greater than a prescribed maximum, respectively.

A simple cloning procedure is used in the present study. When the number of particles in a cell becomes smaller than a prescribed threshold value, the particle having the highest mass is found and split into two daughter particles each having the same properties but half of the mass of the parent particle. The new particles are initially located at the same position but they drift away quickly due to the random walk term in Equation (14). The cloning procedure is repeated until the number of particles in the cell exceeds the threshold value. We note that the cloning does not change the local PDF of the particle properties [14].

Particles are combined in cells having more particles than a prescribed threshold value. When the number of particles in a cell becomes larger than the prescribed threshold value, the particle having the lowest mass is first found, say particle A. Then the particle B that is the closest to A in physical space is determined. The survivor particle is determined at random with a probability proportional to its mass. That is, particles A and B have the probabilities $m_A/(m_A + m_B)$ and $m_B/(m_A + m_B)$, respectively, to be retained. If A is selected to survive, we set $m_A = m_A + m_B$ and B is eliminated. The other properties of A are unchanged. We repeat this procedure until the number of particles in the cell becomes smaller than the threshold value. This procedure is simple and maintains the local distribution of particle properties. Its main disadvantage is that while the mass is conserved, the other particle properties are not necessarily conserved at the discrete level.

4. Results and discussion

Computational results for three different turbulent flames are presented in this section to demonstrate the performance of the hybrid LES/PDF solver. The first test case, the piloted methane/air jet diffusion flame (Sandia Flame-D) [38], is used to examine the consistency, accuracy and efficiency of the hybrid algorithm. First, the LES and PDF algorithms are one-way coupled to investigate the consistency between the two solvers and to examine the performance of the velocity interpolation and correction algorithms in detail. Then the LES and PDF solvers are fully two-way coupled and extensive simulations are performed using a detailed chemical mechanism. In this case, the results are compared with the experimental measurements as well as with the previous LES/PDF simulations. Finally, the performance of the LES/PDF solver is discussed for the computational efficiency. The turbulent non-swirling premixed and swirling stratified flames from the Cambridge turbulent stratified flame series [24,39] are used to demonstrate the accuracy and robustness of the method. The results are compared with the experimental data as well as the LES simulations of Proch and Kempf [40] that are available only for the turbulent non-swirling cases.

4.1. *The piloted methane/air jet diffusion flame*

The first test case deals with a piloted methane/air jet diffusion flame (Sandia Flame-D [38]). In this flame, the burner consists of a central fuel jet surrounded by an annular pilot. An air-coflow surrounds both the pilot and the fuel jets. The fuel jet is a mixture of 25% methane and 75% air by volume. The pilot flame is a lean (the equivalence ratio, $\varphi = 0.77$) mixture of C_2H_2, H_2, air, CO_2 and N_2 with the same equilibrium composition as methane/air at this equivalence ratio, and with a temperature of 1880 K. The fuel nozzle diameter is $D = 7.2$ mm and is enclosed by a broad pilot nozzle with a diameter of $D_p = 2.62D$ and an air-coflow. The inner and outer diameters of the pilot annulus are 7.7 and 18.2 mm, respectively. The jet bulk velocity is $U_j = 49.6$ m/s corresponding to the Reynolds number of Re $= 22,400$, temperature is 294 K and pressure is 0.993 atm. The pilot and coflow bulk velocities are 11.4 and 0.9 m/s, respectively. More details about this flame are available in Barlow et al. [38].

The computational domain is selected to be $[0, 60D] \times [0, 20D] \times [0, 2\pi]$ in the axial (x), radial (r) and azimuthal (θ) directions, respectively. The domain is discretised using a non-uniform $256 \times 128 \times 32$ block-structured cylindrical grid as shown in Figure 4. The grid is concentrated near the nozzle in the axial and radial directions.

The filtered inlet velocities of the fuel jet are obtained from a separate LES turbulent pipe flow simulation. For this purpose, a LES simulation is performed for a turbulent pipe flow with the same dimensions as the fuel jet inlet. In the pipe flow simulation, flow is initialised to have the experimentally measured mean velocity profile at the fuel jet inlet with small random perturbations. The periodic boundary conditions are applied at the inlet and outlet, and no-slip boundary conditions are used at the wall of the pipe. The pipe flow simulation is first performed until the turbulent flow reaches a statistically stationary state, and then the flow velocities on a plane perpendicular to the pipe axial direction are stored in a file as time series with a specified time step size. Then the velocities stored in the file are retrieved and interpolated on the grid points in the fuel jet inlet during the LES/PDF simulations. The interpolation is performed using cylindrical coordinates. Note that the
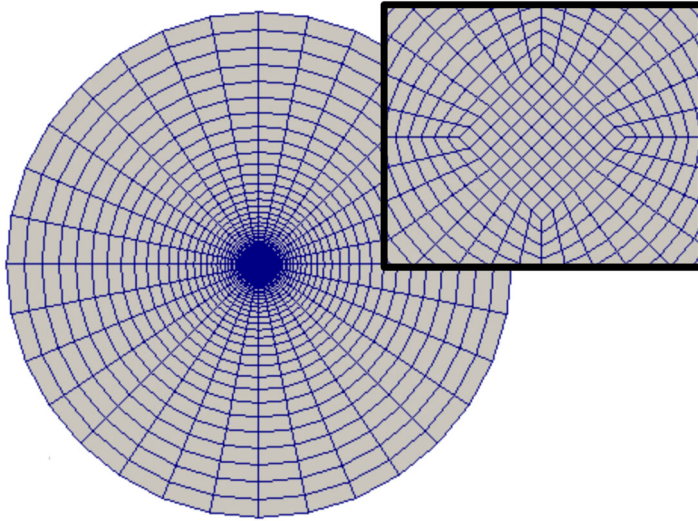

Figure 4. The block-structured grid used in the simulations.

interpolated velocities at the fuel jet inlet may not have the same mean and rms profiles as the experimental measurements at the fuel jet inlet. Therefore, instead of directly using the interpolated velocities, we apply the turbulent inlet velocity at the fuel jet computed as [41]

$$u_i^s(r,\theta,t) = \langle u_i(r)\rangle_m + \alpha_i(r)\left[u_i^l(r,\theta,t) - \langle u_i^l(r)\rangle\right],\tag{37}$$

where $\langle u_i(r)\rangle_m$ and $\langle u_i^l(r)\rangle$ are the mean values of the experimental and the interpolated velocities, respectively, and $u_i^l(r,\theta,t)$ is the interpolated instantaneous velocity while $u_i^s(r,\theta,t)$ is the scaled instantaneous velocity to be used at the fuel jet inlet. The scaling parameter $\alpha_i(r)$ is used to match the interpolated fluctuating velocities with the experimental fluctuating velocities, and it is computed as

$$\alpha_i(r) = \frac{\langle u_i'(r)\rangle_l}{\langle u_i'(r)\rangle_m},\tag{38}$$

where $\langle u_i'(r)\rangle_m$ is the experimental measurement of the rms velocity and $\langle u_i'(r)\rangle_l$ is the rms of the interpolated velocity calculated as

$$\langle u_i'(r)\rangle_l = \sqrt{\langle u_i^l(r,\theta,t)^2\rangle - \langle u_i^l(r)\rangle^2},\tag{39}$$

where the scaling factor α_i varies between $0.94 \leq \alpha_i \leq 0.97$.

At the pilot nozzle exit, we use the experimental mean velocity as the inlet boundary conditions by neglecting the turbulent fluctuations. The inlet velocity of the air-coflow is set to a constant value of 0.9 m/s. At the wall-lips between the fuel jet and pilot flame as well as between the pilot and the coflow, the no-slip boundary conditions are applied. At the outlet, the zero-gradient boundary conditions are used for all the fields. At the far fields, the slip boundary conditions are applied. In the PDF solver, about 20 particles per grid cell are used in all the results presented in this paper. The model constant used in Equation (13) is selected as $C_m = 4$.

4.2. *Consistency between LES and PDF solvers*

The one-way coupling methodology of Wang and Pope [15] is used to examine the numerical consistency between the LES and PDF solvers. In this methodology, as its name implies, the data transfer occurs only in one direction, from the LES solver to the PDF solver. The fields calculated by the PDF solver are used only for the output purpose, i.e. there is no feedback from the PDF solver to the LES solver as schematically shown in Figure 5. The main goal here is to isolate the numerical error caused by the data transfer from the PDF solver to the LES solver.
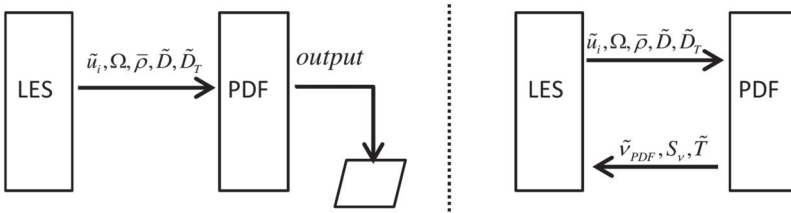

Figure 5. Schematic representation of one-way coupled (left) and two-way coupled (right) LES/PDF solver.

In the PDF solver, all the thermochemical properties such as species mass fractions Y, temperature T, density ρ, etc. are obtained from the mixture fraction ξ using a simple flamelet table, i.e. $\phi = f(\xi)$. With the fields $\bar{\rho}$, $\tilde{D}_T$, $\tilde{u}_i$ being supplied by the LES solver, the PDF method solves the following equations:

$$dX_j^* = \left[\tilde{u}_j + \frac{1}{\bar{\rho}} \frac{\partial(\bar{\rho}\tilde{D}_T)}{\partial x_j}\right]^* dt + \left[2\tilde{D}_T^*\right]^{1/2} dW_j^*, \tag{40}$$

$$d\xi^* = -\Omega^*(\xi^* - \tilde{\xi}^*) \, dt + \left[\frac{1}{\bar{\rho}} \frac{\partial}{\partial x_j}\left(\bar{\rho}\tilde{D}\frac{\partial\tilde{\xi}}{\partial x_j}\right)\right]^* dt. \tag{41}$$

The implied transport equations for the filtered mixture fraction $\tilde{\xi}$ and the squared mixture fraction $\widetilde{\xi^2}$ can be directly derived from Equations (40) and (41) to obtain

$$\frac{\partial\left(\bar{\rho}\tilde{\xi}\right)}{\partial t} + \frac{\partial\left(\bar{\rho}\tilde{u}_j\tilde{\xi}\right)}{\partial x_j} = \frac{\partial}{\partial x_j}\left(\bar{\rho}\left(\tilde{D} + \tilde{D}_T\right)\frac{\partial\tilde{\xi}}{\partial x_j}\right), \tag{42}$$

$$\frac{\partial\left(\bar{\rho}\widetilde{\xi^2}\right)}{\partial t} + \frac{\partial\left(\bar{\rho}\tilde{u}_j\widetilde{\xi^2}\right)}{\partial x_j} = \frac{\partial}{\partial x_j}\left(\bar{\rho}\tilde{D}_T\frac{\partial\widetilde{\xi^2}}{\partial x_j}\right) + 2\tilde{\xi}\frac{\partial}{\partial x_j}\left(\bar{\rho}\tilde{D}\frac{\partial\tilde{\xi}}{\partial x_j}\right)$$
$$- 2\bar{\rho}\Omega\left(\widetilde{\xi^2} - \tilde{\xi}^2\right), \tag{43}$$

which are solved by the LES solver. In the LES solver, it is assumed that the PDF of ξ is a β-function determined by the filtered mixture fraction $(\tilde{\xi})$ and variance of mixture fraction $(\widetilde{\xi''^2} = \widetilde{\xi^2} - \tilde{\xi}^2)$. Then the filtered compositions $\tilde{\phi}$ are obtained from a lookup table based on $\tilde{\xi}$ and $\widetilde{\xi''^2}$, i.e. $\tilde{\phi} = G(\tilde{\xi}, \widetilde{\xi''^2})$. We note that the equations for $\tilde{\xi}$ and $\widetilde{\xi^2}$ solved in the LES solver and implied by the PDF solver are identical. Hence any differences in the results are due entirely to numerical error. On the other hand, differences between the other thermochemical properties such as $\tilde{T}$, T'', $\tilde{Y}$ and Y'' obtained from the two solvers may be due in part to the differences between the PDF of ξ calculated with the PDF solver and the β-distribution assumed in the LES solver.

In the one-way coupled LES/PDF simulations, the fields of the resolved mixture fraction, $\tilde{\xi}$, square of mixture fraction, $\widetilde{\xi^2}$ and temperature, $\tilde{T}$, are computed redundantly by the LES and PDF solvers. The LES and PDF fields are time averaged after a statistically stationary state is reached and the time-averaged quantities are denoted by $\langle\cdot\rangle$.

We first present the radial profiles of the time-averaged resolved axial velocity $\langle\tilde{U}\rangle$ and rms fluctuating axial velocity $\langle u''\rangle$ to show that the flow fields are well captured in the simulations and then the time-averaged LES and PDF results of the resolved mixture fraction, $\langle\tilde{\xi}\rangle$, the resolved temperature, $\langle\tilde{T}\rangle$, the rms of mixture fraction $\langle\xi''\rangle = (\langle(\tilde{\xi})^2\rangle - \langle\tilde{\xi}\rangle^2)^{1/2}$ and the rms of temperature, $\langle T''\rangle$ to demonstrate the numerical consistency. Figure 6 shows the time-averaged profiles of the LES and PDF fields with the experimental measurements at the axial locations $x/D = 7.5, 15, 30$ and 45. As can be seen in this figure, the mean axial velocity and rms fluctuating axial velocity are in good agreement with the experimental data, showing that the flow fields are well captured. The time-averaged resolved mixture fraction $\langle\tilde{\xi}\rangle$ and the rms of mixture fraction $\langle\xi''\rangle$ from the LES and PDF solvers are
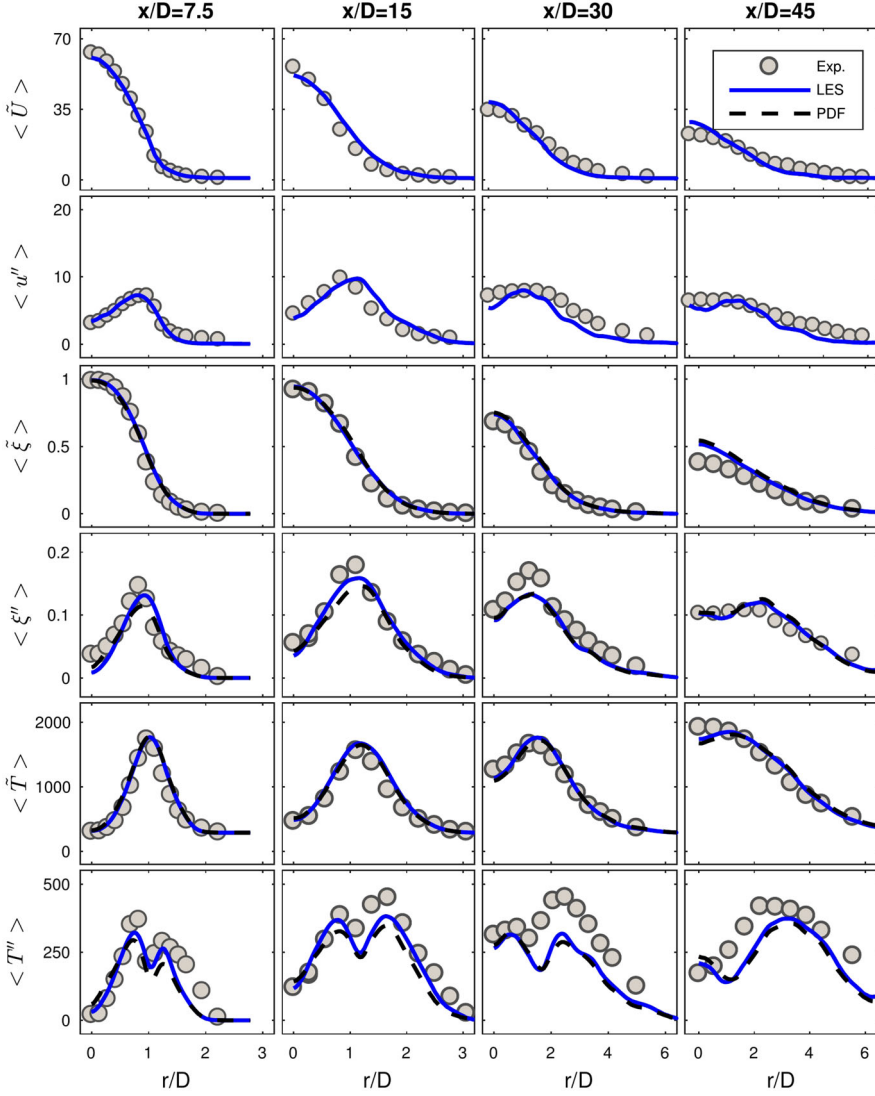
Figure 6. The one-way coupling. The radial profiles of time-averaged resolved axial velocity, rms fluctuating axial velocity, resolved mixture fraction, rms of mixture fraction, resolved temperature and rms of temperature, from top to bottom at the axial locations $x/D = 7.5, 15, 30$ and 45 from left to right. Symbols, the experimental data; solid line, the LES results; dashed line, the PDF results. (Colour online.)

also compared to show the consistency. As seen, the LES and PDF results are in excellent agreement, demonstrating that the LES and PDF solvers are consistent at the numerical solution level. Note that this consistency also indicates the accuracy of the numerical algorithms used in the PDF solver, i.e. the particle tracking, mean estimation and interpolation methods. The time-averaged resolved temperature $\langle \tilde{T} \rangle$ from the LES and PDF solvers are almost identical while very slight discrepancies occur in the rms of the temperature $\langle T'' \rangle$ fields obtained by the two solvers, which demonstrates high level of consistency at the

numerical-solution level. As mentioned above, the slight differences in $\langle \tilde{T} \rangle$ and $\langle T'' \rangle$ may be due in part to the different PDFs of ξ in the LES and PDF solvers. Although, a simple flamelet model is used in the simulations, the agreement with the experimental data is also very good.

4.3. *Detailed chemistry calculations*

The detailed chemistry simulations are performed using the augmented reduced mechanism (ARM1) that includes 16-species and 12-reactions [42]. Unity Lewis number assumption is applied for all species, thus the differential diffusion is not taken into account. Here the fully two-way coupled LES/PDF solver is used, hence removing the assumption of a β-function PDF of mixture fraction. In the PDF solver, each particle carries the mass fractions of chemical species and the enthalpy. Figure 7 shows the computational modules used in the detailed chemistry calculations. The LES component solves the filtered mass, the filtered momentum and the specific volume transport equations, and then the PDF solver performs the steps 1 and 2 in the $\mathbb{TMR}$ fractional time stepping method while the third step is performed by the ISAT module. The simulations are performed for 10 flow-through times based on jet bulk velocity to reach a statistically stationary state, then an additional 10 flow-through times are performed to collect the statistics from the instantaneous resolved fields. For instance, the instantaneous resolved temperature field is shown in Figure 8.

   Figure 9 presents the time-averaged radial profiles of the resolved temperature, $\langle \tilde{T} \rangle$, and resolved species mass fractions, $\langle \tilde{Y} \rangle$, of CO_2, CO, O_2 and CH_4 at the axial locations $x/D = 7.5, 15, 30$ and 45. The numerical results are compared with the experimental data as well as with the results from a previous LES/PDF simulation [43] at the locations where they are available. It is emphasised here that the previous LES/PDF simulations were performed on a non-uniform $192 \times 192 \times 96$ cylindrical grid using a one-way coupled LES/PDF solver [15] with the modified Curl mixing model [44] and the 38-species C_1–C_4 skeletal mechanism [45]. Thus the previous simulation results are used here only as a reference. As seen in Figure 9, the results are in very good agreement with the experimental data at $x/D = 7.5$ and 15. At $x/D = 30$, the experimental data are reproduced with a slight discrepancy close to the centre line. However, the trend in the results is consistent with the trend observed in the previous LES/PDF simulations. At $x/D = 45$, although the trends are similar in the present and the previous LES/PDF simulations, the discrepancy between experimental data and the numerical results is visible.

   Figure 10 shows the rms of temperature, $\langle T'' \rangle$, and species mass fractions, $\langle Y'' \rangle$, of CO_2, CO, O_2 and CH_4 together with the experimental data and the results from the previous LES/PDF simulations. Similar observations can be made for the rms values. At the locations $x/D = 7.5$ and 15, the present LES/PDF results are in good agreement with the experimental data and markedly better than the previous LES/PDF simulations of Hiremath et al. [43]. At the locations $x/D = 30, 45$ the rms values of the present and previous

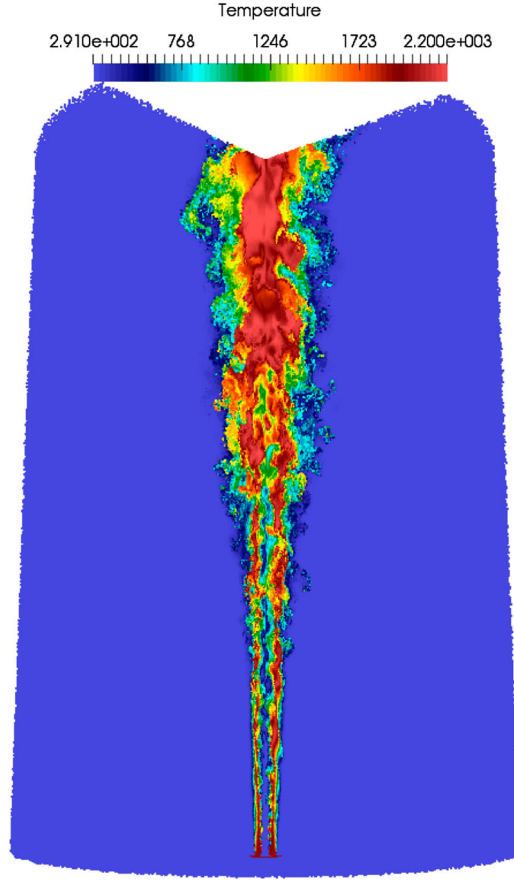Figure 7.   The computational modules used in the detailed chemistry calculations.

Figure 8. 3D plot of Lagrangian particles in the Sandia Flame-D simulations that are coloured by the instantaneous temperature at a time step after reaching a statistically stationary state. (Colour online.)

LES/PDF simulations have very similar trends: They both slightly underpredict the rms values compared to the experimental measurements. However, at the location $x/D = 45$, close to the centreline, the rms profile of CH_4 is significantly higher than both the experimental data and the previous PDF simulation, which is partly attributed to the different chemical mechanism used in the present simulations.

4.4. *Performance of the velocity interpolation and correction method*

In this section, we investigate the performance of the three-stage velocity interpolation and correction algorithm in enforcing the consistency between the particle mass density, ρ_P^k, defined as the total particle mass in the kth cell divided by the volume of the cell, and the finite-volume density, ρ_{FV}^k, at the numerical solution level. It is emphasised here that this is the first detailed investigation of the three-stage velocity interpolation and correction algorithm in the context of the LES/PDF method applied to complex reacting flows of practical interest. Its performance is assessed through extensive simulations of a turbulent piloted jet diffusion flame (Sandia Flame-D) using the fully two-way coupled
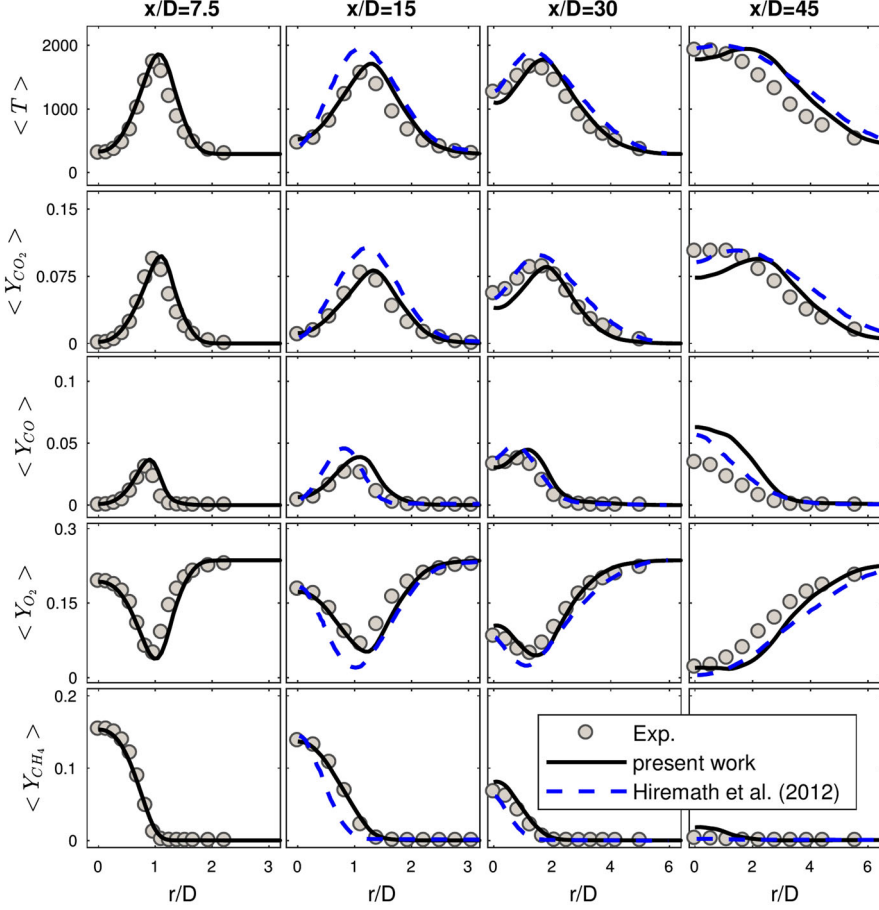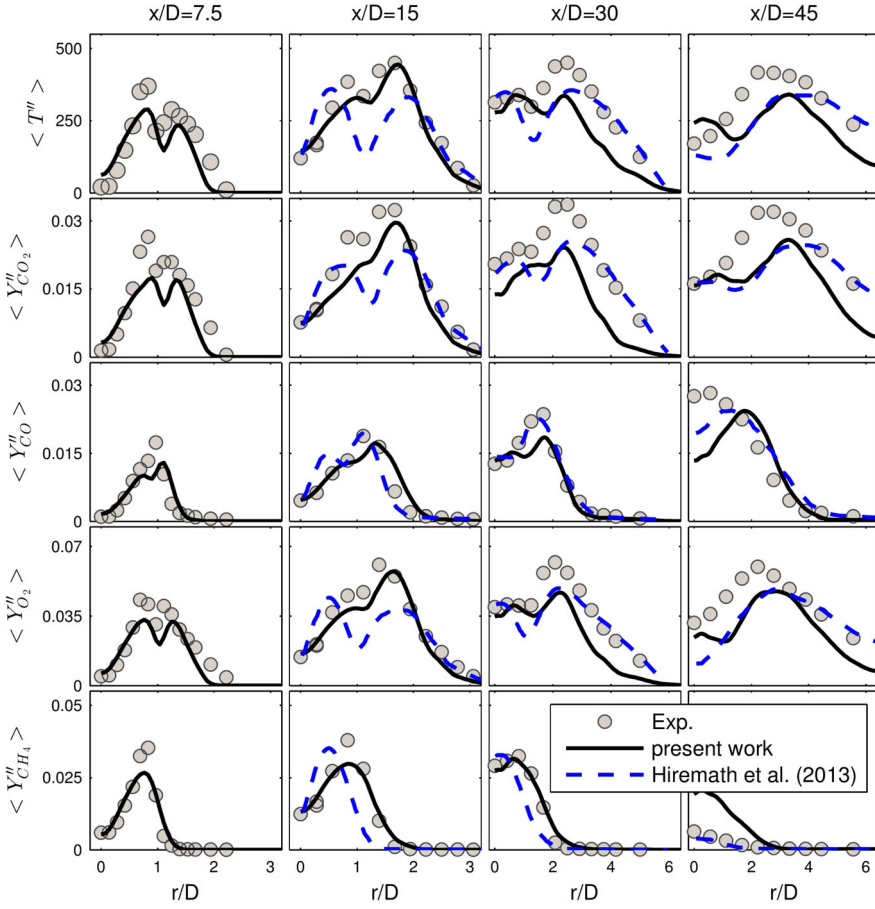
Figure 9. Radial profiles of time-averaged resolved temperature T and resolved species mass fractions of CO_2, CO, O_2 and CH_4 from top to bottom, at axial locations $x/D = 7.5, 15, 30$ and 45, from left to right. Symbols, the experimental data; solid line, the present LES/PDF simulation; dashed line, the previous LES/PDF simulation. (Colour online.)

LES/PDF solver. First, the performance of each stage is examined separately and then the performance of the three stages is demonstrated.

The consistency is quantified using the deviation between the particle mass density (i.e. the total mass of particles in a cell divided by the cell volume) ρ_P, and the finite-volume density, ρ_{FV}. For the kth cell, the deviation is defined as [11]

$$\epsilon_\rho^k \equiv \frac{\rho_P^k - \rho_{FV}^k}{\rho_{FV}^k}. \tag{44}$$

The global consistency is then quantified by taking the rms of ϵ_ρ^k over the entire computational domain as [11]

$$\epsilon_{rms}^\rho \equiv \left(\frac{\sum_{k=1}^{N_C} \left(\epsilon_\rho^k \right)^2}{N_C} \right)^{1/2}, \tag{45}$$

Figure 10. Radial profiles of time-averaged the rms of temperature and the rms of species mass fractions of CO_2, CO, O_2 and CH_4 from top to bottom, at axial locations $x/D = 7.5, 15, 30$ and 45, from left to right. Symbols, the experimental data; solid line, the present LES/PDF simulation; dashed line, the previous LES/PDF simulation. (Colour online.)

where N_C is the total number of grid cells used in the simulation. It should be appreciated that the 'optimal' value of ϵ_{rms}^ρ is not zero. With relatively few particles per cell ($N_{pc} \approx 20$), significant statistical fluctuations are to be expected, e.g. of order $N_{pc}^{-1/2}$, or about 20%.

First, the two-way coupled simulations are performed using the detailed chemistry mechanism to demonstrate the performance of the velocity interpolation and correction algorithm. Figure 11 shows a contour plot of the instantaneous deviation between particle mass and FV densities on the plane passing through the fuel jet axis. The simulations are repeated using no correction (Stage 1), the first-level correction (Stages 1 and 2), and the second-level correction (Stage 1–3) with two different relaxation time parameters of $\alpha = 25$ and $\alpha = 100$. In the simulations with no correction (Stage 1), the deviations between the particle mass and FV densities are very large. The deviations are significantly reduced when the first-level correction is used (Stage 1 and 2). The improvement in the particle mass distribution with Stage 1 and 2 shows the importance of Stage 2 correction step. Although the first-level correction (Stages 1–2) greatly reduces the deviations, there

still remains some deviations between the particle mass and FV densities. The second-level correction (Stages 1–3) virtually eliminates the deviations when an optimal or a nearly optimal value of α is used, and this results in very good consistency between the two density fields.

The relaxation parameter is expected to be critically important in maintaining numerical stability and accuracy of the LES/PDF simulations. To determine its influence on the numerical stability and the satisfaction of the consistency conditions, simulations are performed using $\alpha = 1, 10, 25$ and 100. It is found that a numerical instability arises for the cases of $\alpha = 1$ and $\alpha = 10$ due to excessive correction velocities that become as large as the jet velocity at the inlet. Therefore the simulations are completed only for the values of $\alpha = 25$ and 100 without any instability problem. As can be seen in Figure 11, the deviations in the density fields computed with $\alpha = 25$ are smaller than those computed with $\alpha = 100$. As expected, using a smaller relaxation time scale results in a better consistency between the particle mass and FV density fields. On the other hand, a too small relaxation time scale tends to result in a numerical instability due to the excessive corrections. In addition, although not shown here, excessive corrections lead to significant inaccuracies in other quantities, e.g. particularly in the filtered mean and the rms of the fluctuating velocity profiles. There is a trade off between the accuracy, consistency and numerical stability, and thus the relaxation time scale should be selected carefully such that the consistency condition is effectively enforced while the numerical stability, accuracy and robustness are maintained even in severe cases.

Figure 12 shows the time evolution of the rms of the deviation between particle mass and FV densities in the simulations with (i) no correction (Stage 1), (ii) the first-level correction (Stage 1 and 2), (iii) the second-level correction (Stages 1–3) with time relaxation parameter of $\alpha = 25$ and (iv) the second-level correction (Stages 1–3) with time relaxation parameter of $\alpha = 100$. The simulation with no correction results in the highest deviation with about $\epsilon_{rms}^{\rho} = 0.4$. Moreover, ϵ_{rms}^{ρ} continues to increase slightly as the simulation proceeds even after a statistically stationary state is reached. The first-level correction (Stages
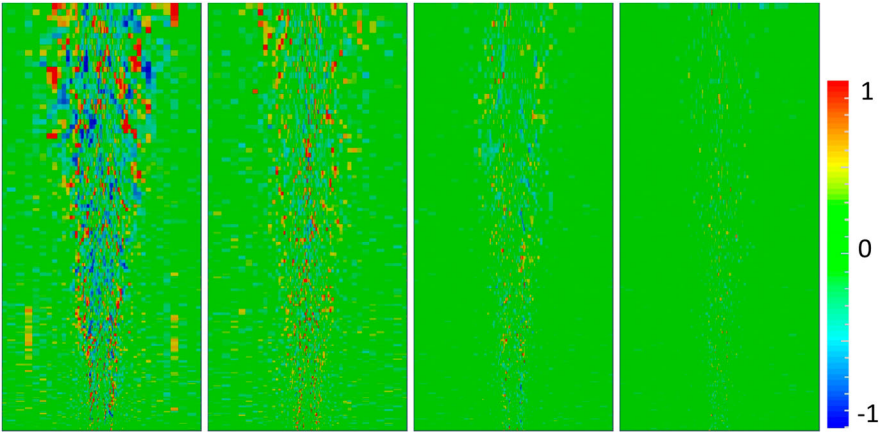

Figure 11. The deviation ϵ_{ρ}^{k} between particle mass density and FV density fields computed using (from left to right) no correction (Stage 1), the first-level correction (Stages 1 and 2), and the second-level correction (Stages 1–3) with time relaxation parameter of $\alpha = 100$, and the second-level correction (Stages 1–3) with time relaxation parameter of $\alpha = 25$. (Colour online.)
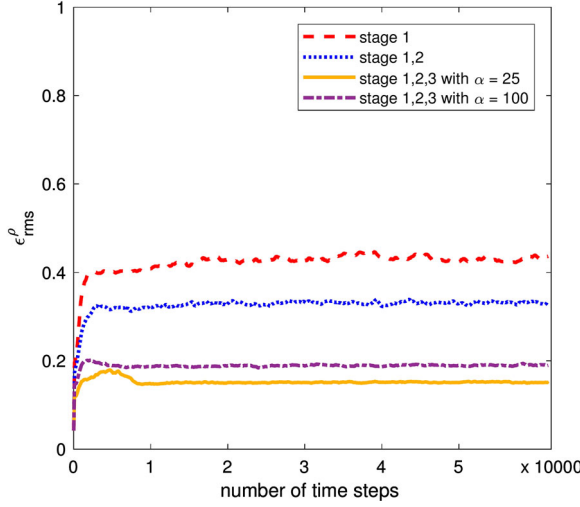
Figure 12. The time evolution of the rms of deviation between particle mass and FV densities ϵ_{rms}^{ρ}. Dashed line, no correction (Stage 1); dotted line, the first-level correction (Stage 1 and 2); dash-dot line, the second-level correction (Stages 1–3) with $\alpha = 100$; solid line, the second-level correction (Stages 1–3) with $\alpha = 25$. (Colour online.)

1 and 2) reduces the value of ϵ_{rms}^{ρ} by 25% compared to the case of no correction applied. Additionally, ϵ_{rms}^{ρ} does not seem to increase during the simulation in this case. When the second-level correction (Stages 1–3) is turned on, ϵ_{rms}^{ρ} is reduced below 0.2 for both $\alpha = 25$ and $\alpha = 100$ cases. It can be also seen that the second-level correction with $\alpha = 25$ results in a smaller ϵ_{rms}^{ρ} than that with $\alpha = 100$. Moreover, ϵ_{rms}^{ρ} does not increase after an initial period, i.e. after about 10,000 time step, in both cases of $\alpha = 25$ and $\alpha = 100$.

Then the one-way coupled simulations are also carried out to better show the performance of the three-stage correction algorithm in fulfilling its main duty of consistently interpolating the LES velocity field onto particles. For this purpose, the three-stage velocity correction method is incorporated into the one-way coupled LES/PDF solver and simulations are performed for the Sandia Flame-D case using various stages of the three-stage velocity correction algorithm. In particular, one-way coupled simulations are carried out using (i) no correction (Stage 1), (ii) the first-level correction (Stage 1 and 2), (iii) the second-level correction (Stages 1–3) with time relaxation parameter $\alpha = 25$ and (iv) the second-level correction (Stages 1–3) with time relaxation parameter $\alpha = 100$ and the results are compared for the consistency between the LES and particle fields.

The time-averaged resolved mixture fraction is compared first along the centreline, and then at the axial locations of $x/D = 30$ and 45. Figure 13 shows the time-averaged resolved mixture fraction computed by the LES and PDF solvers along the centreline. As may be seen, the results obtained by the PDF solver with no correction (Stage 1) deviate significantly from the LES results. The first-level correction (Stages 1 and 2) greatly improves the consistency between the LES and PDF results, but very slight discrepancies appear especially between $x/D = 15$ and 30. These discrepancies are completely removed when the second-level correction (Stages 1–3) with $\alpha = 25$ is applied, yielding excellent agreement between the LES and PDF fields.

To show the effects of the relaxation time, simulations are also performed for $\alpha = 25$ and $\alpha = 100$, and the results are compared in Figure 14. This figure shows that the second-level
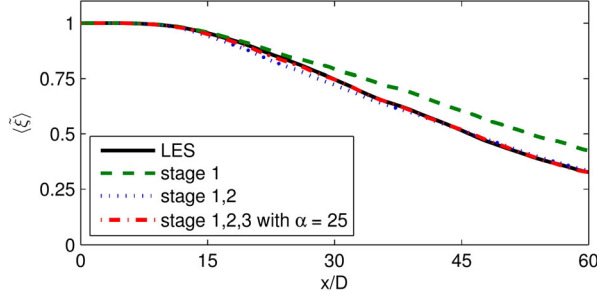
Figure 13.   The LES and PDF results of the time-averaged resolved mixture fraction along the centreline for the Sandia Flame-D. Solid line, LES; dashed line, PDF with no correction (Stage 1), dotted line, PDF with the first-level correction (Stages 1 and 2), dash-dot line, PDF with the second-level correction (Stages 1–3) with $\alpha = 25$. (Colour online.)
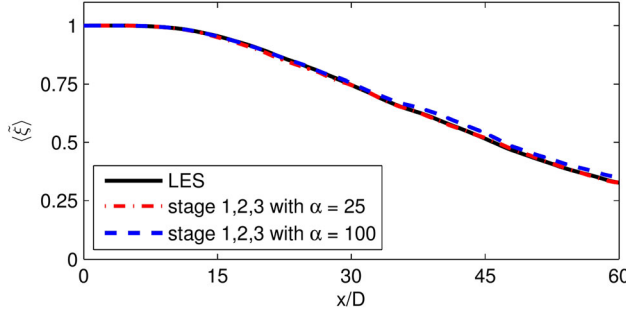

Figure 14.   The LES and PDF results of the time-averaged resolved mixture fraction along the centreline for the Sandia Flame-D. Solid line, LES; dashed line: PDF with the second-level correction (Stage 1–3) with $\alpha = 100$; dash-dot line, PDF with the second-level correction (Stages 1–3) with $\alpha = 25$. (Colour online.)

correction yields overall good consistency even for $\alpha = 100$. However the discrepancy slightly decreases for $\alpha = 25$.

The radial profiles of the time-averaged resolved mixture fraction $\langle \tilde{\xi} \rangle$ from the LES solver and the PDF solver using different levels of correction are plotted in Figure 15. As seen, the results from the PDF solver using only the first-level correction (Stages 1 and 2) are in very good agreement with the LES results. At $x/D = 30$, the PDF results are slightly smaller than the LES results close to the centreline. In the case of no correction (Stage 1), there is significant discrepancy between the LES and the PDF results.

In summary, the first-level (Stage 1 and 2) and the second-level (Stage 1–3) corrections significantly improve the consistency between the LES and PDF solvers. For the Sandia Flame-D case, the second-level correction results in about 50% less error compared to the first-level correction in terms of the rms of deviations between the particle and FV density fields. The one-way coupled LES/PDF simulations of the Sandia Flame-D with the first-level and the second-level corrections indicate that both levels yield good consistency between the LES and PDF fields. However, the simulation with the second-level correction results in a slightly better consistency. As discussed before, the time relaxation parameter α used in the second-level correction algorithm must be selected carefully for the best
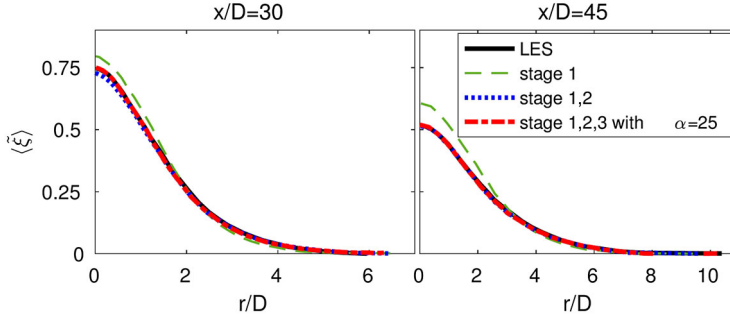
Figure 15. The LES and PDF results of the radial profiles of the time-averaged resolved mixture fraction at $x/D = 30$ (left) and at $x/D = 45$ (right) for the Sandia Flame-D. The solid lines, LES; the dashed lines, PDF with no correction (Stage 1); the dotted lines, PDF with the first-level correction (Stage 1 and 2); the dash-dot lines, PDF with the first and second-level corrections (Stage 1–3) with $\alpha = 25$. (Colour online.)

performance. We recommend to use $\alpha = 100$ as a default value if it is to be used by a non-expert. For this value, the second-level correction is found to perform well independent of grid size for the test cases considered in the present study.

4.5. *Computational cost*

The computational cost is examined in this section. For this purpose, the fully two-way coupled LES/PDF simulations with the ARM1 reduced mechanism are performed using a $256 \times 128 \times 32$ cylindrical block-structured grid as shown in Figure 4 with about 20 particles per cell. The computational domain is decomposed into 96 subdomains and the simulations are carried out for 10 flow-through times based on the fuel jet bulk velocity to reach a statistically stationary state, and then an additional 10 flow-through times were performed to collect the statistics. In total, about 100,000 time steps are marched in each simulation. The simulations with detailed chemistry representation using ISAT are completed in 7 days wall-clock time using 96 cores. The total computational wall-clock time is approximately 37 μs/particle/timestep.

The relative computational cost of each component of the LES/PDF simulations is presented in Figure 16. As can be seen in this figure, about 85% of the total computational time is consumed by the PDF solver. Thus the cost of the LES/PDF calculations is less than 7 times the cost of the LES alone. This is quite reasonable considering that the joint PDF of 16 reactive species is being calculated, compared to 3 velocity components in the LES solver. Additionally, 85% of the computational time of the PDF solver is consumed by the three main processes of transport $\mathbb{T}$, mixing $\mathbb{M}$ and reaction $\mathbb{R}$. The reaction module of the PDF solver consumes about 30% of the total computational time whereas the mixing and transport processes consume about 20% and 22% of the total computational time, respectively. The remaining 15% of the computational time of the PDF solver is mainly required for the calculation of statistical moments from the particles. The computational time required by the new LES/PDF solver is of the same order of those reported in the previous LES/PDF simulations [6,7,15].

We also examine the computational cost of the three-stage velocity interpolation and correction method. The computational cost required by each stage in the method is investigated separately. Here, we first define the computational cost of using each stage of the
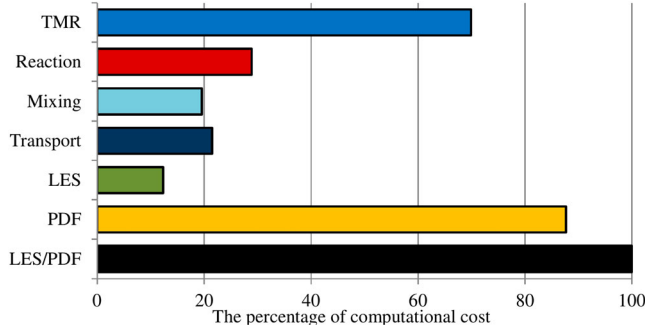
Figure 16. The percentage of the computational cost of LES and PDF solver as well as the transport $\mathbb{T}$, mixing $\mathbb{M}$ and reaction $\mathbb{R}$ calculations in PDF solver. $\mathbb{TMR}$ represents the total percentage of elapsed time of transport, mixing and reaction in PDF solver. (Colour online.)
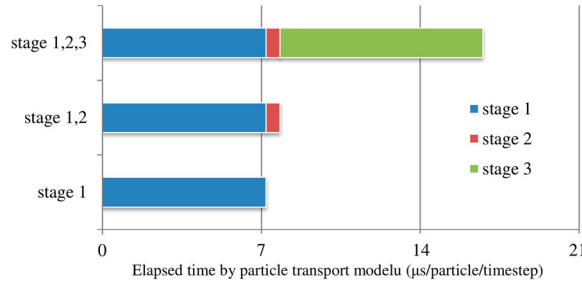

Figure 17. The elapsed time by the particle transport module in the PDF solver per particle per time step. (Colour online.)

velocity correction method, and then give the relative cost of each stage. The cost for Stage 1 consists of the cost of interpolation of the LES velocities first from the cell centres to the cell vertices and then from cell vertices onto the particle locations, and the cost of tracking particles in the computational domain. The cost of the Stage 2 correction mainly occurs due to solution of a linear system of equations for each cell. The Stage 3 requires solution of a large linear system of equations similar to the discrete pressure Poisson equation to obtain the Stage 3 velocity corrections at the cell centres, and then moving the particles with this correction velocity using the Stage 1 and 2. In Figure 17, the time consumed by each stage is presented. As seen, the Stage 1 requires a considerable amount of time since it performs the tracking of the particles in the computational domain. The additional cost for using the Stage 2 correction is about 8% of the cost of the Stage 1. However, using the Stage 3 correction requires more than the total cost of Stage 1 and 2.

5. The Cambridge stratified methane/air flames

The fully two-way coupled hybrid LES/PDF solver is finally applied to turbulent non-swirling premixed and swirling stratified methane/air flames from the Cambridge stratified swirl flames series to demonstrate the predictive capability and robustness of the numerical method for these challenging test cases. The Cambridge/Sandia swirl burner was designed to investigate the effect of the stratification in the non-swirling and swirling operating conditions. Here, we consider two different flames: the non-swirling premixed flame

Table 1. The equivalence ratios and swirl numbers in the annular jets.

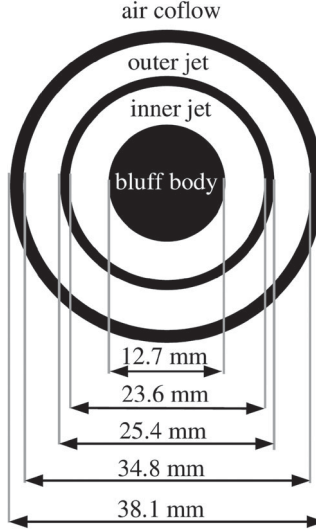| Case	φ_{inner}	φ_{outer}	$\varphi_{inner}/\varphi_{outer}$	$S = U_{tg}/U_z$	
SwB1	0.75	0.75	1	0	(no-swirl)
SwB6	1	0.5	2	0.45	

Figure 18. A schematic of the stratified bluff-body burner [24].

labelled as *SwB1*, and the moderately stratified and moderately swirling flame labelled as *SwB6*. The operating conditions for both flames are summarised in Table 1 where the swirl number, *S*, is defined as the ratio of measured mean tangential velocity to axial velocity, $S = U_{tg}/U_z$, above the centre of the outer fuel jet [39]. The schematic of the burner is shown in Figure 18. The burner consists of a central bluff body surrounded by two annular fuel jets, i.e. the inner and the outer jets. In the outermost annulus, air-coflow is supplied to prevent entrainment of the ambient air. The bluff-body diameter is $D_b = 12.7$ mm, the inner jet annulus diameter is 23.6 mm with the wall thickness of 0.9 mm, and the outer jet annulus diameter is 34.8 mm with the wall thickness of 0.9 mm. In the inner and outer jets, the inlet bulk velocities are 8.31 and 18.7 m/s corresponding to the Reynolds numbers of 5960 and 11,500, respectively, and the air-coflow has a laminar inlet velocity of 0.4 m/s.

The flames are stabilised by a recirculation created behind the bluff body. The velocity measurements are provided by Zhou et al. [46], and the temperature and mass fraction measurements by Sweeney et al. [24,39].

The cylindrical computational domain spans 200 mm in the axial *x*-direction and 200 mm in the radial *r*-direction. The domain is discretised using a non-uniform $192 \times 128 \times 96$ block-structured cylindrical grid. The grid is concentrated near the nozzle in the axial direction and in the shear layer between the fuel jets in the radial direction.

In the fuel jets, the instantaneous inlet velocities are obtained from two separate turbulent annular pipe flow simulations. We use the same method as explained in the previous section for interpolation of the inlet velocities from the turbulent pipe flow simulations, and

the scaling factor α_i varies between $0.96 \leq \alpha_i \leq 0.98$. The inlet velocity of the air-coflow is set to the uniform velocity profile of $0.4\,\text{m/s}$. At the bluff body and wall-lips, no-slip boundary conditions are applied. The zero-gradient boundary conditions are imposed for all the fields at the outlet and at the far field, i.e. on the lateral surface. About 20 particles per cell are used in the PDF solver. The methane/air combustion is represented by the augmented reduced mechanism (ARM1) [42]. Unity Lewis number assumption is applied for all the species. ISAT is employed to accelerate the chemical kinetic calculations. The mixing model constant is selected as $C_m = 20$ and 45 for *SwB1* and *SwB6*, respectively, based on the numerical experimentation. Only the first-level velocity correction method
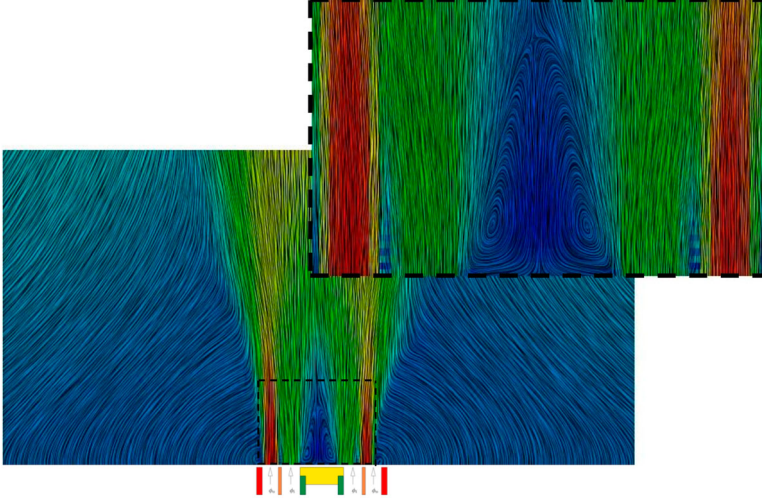
Figure 19. Time-averaged streamlines computed by the present hybrid LES/PDF solver for the *SwB1* case superimposed on the magnitude of the time-averaged resolved axial velocity. (Colour online.)
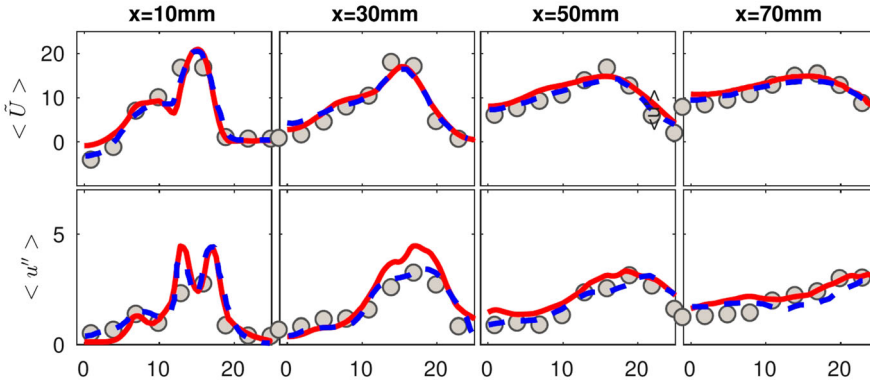
Figure 20. *SwB1*: The radial profiles of time-averaged resolved axial velocity (top) and rms fluctuating axial velocity (bottom) at axial locations $x = 10$, 30, 50 and 70 mm. The symbols: The experimental data; solid line: LES/PDF results; dashed line: results by Proch and Kempf [40]. (Colour online.)

is employed in the simulations. The simulations are parallelised by domain decomposition technique using 192 cores. A constant time step of $\Delta t = 2 \times 10^{-6}$ s is used in the simulation corresponding to the Courant number of about 0.15.

5.1. *The non-swirling premixed flame, SwB1*

The numerical results from the simulations of the non-swirling premixed case (*SwB1*) are presented in this section. Figure 19 shows the time-averaged streamlines to demonstrate the general flow pattern and the recirculation zone behind the bluff body. The length of the recirculation zone is found to be about 22 mm which is very consistent with the experimental value of about 24 mm. Figure 20 shows the time-averaged radial profiles of resolved axial mean velocity $\langle \tilde{U} \rangle$ and the rms fluctuating axial velocity $\langle u'' \rangle$ at the axial locations
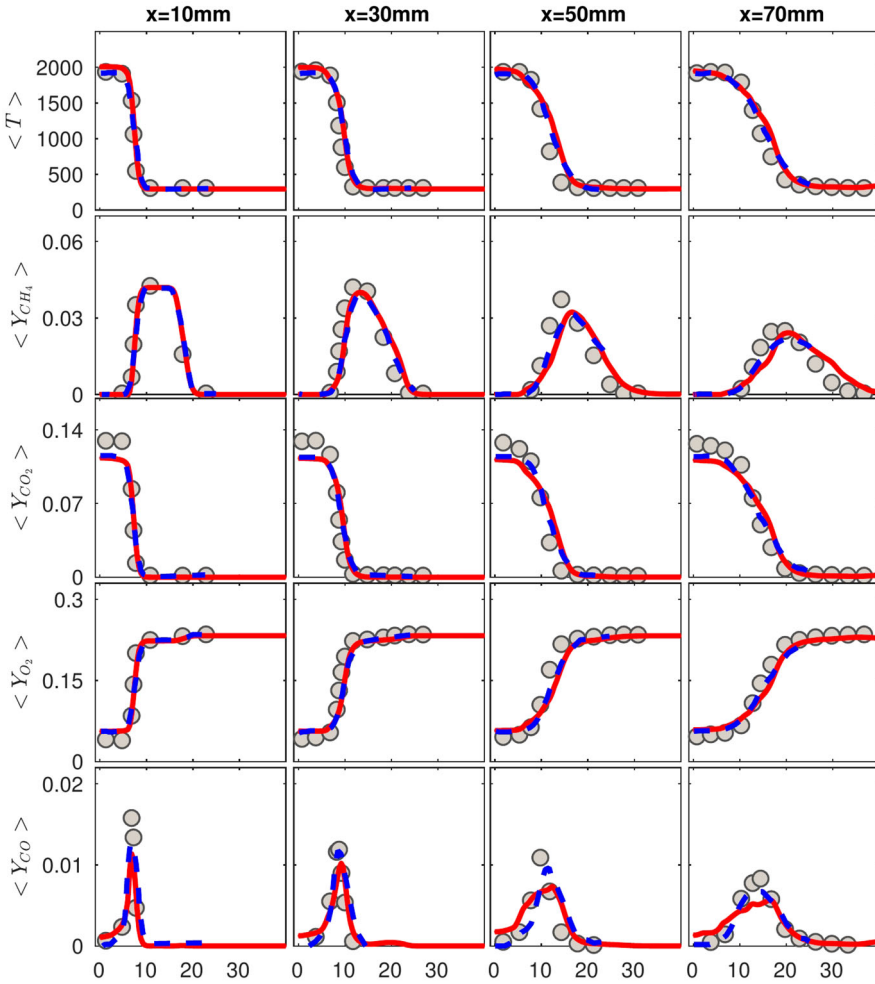
Figure 21. *SwB1*: The radial profiles of the time-averaged resolved temperature and the resolved mass fractions of CH_4, CO_2, O_2 and CO at the axial locations of $x = 10, 20, 30, 50$ and 70 mm. The symbols: the experimental data; the solid line: the LES/PDF results; the dashed line: the results by Proch and Kempf [40]. (Colour online.)

$x = 10, 30, 50$ and $70\,mm$. As seen, the mean axial velocity profiles are in good agreement with the experimental measurements as well as with the previous LES simulation by Proch and Kempf [40] at all the locations.

Figure 21 shows the time-averaged radial profiles of the resolved temperature $\langle \tilde{T} \rangle$ and mass fractions of CH_4, CO_2, O_2 and CO at the axial locations $x = 10, 30, 50$ and $70\,mm$. The temperature profiles are in very good agreement with the experimental data and the previous LES results [40] at all the axial locations. Overall the mass fraction profiles are well predicted at all locations and the present results are in good agreement with the LES simulations of Proch and Kempf [40].

Finally, the radial profiles of the rms fluctuating temperature and the rms fluctuating mass fractions of CH_4, CO_2, O_2 and CO are shown in Figure 22. As seen, the rms profiles
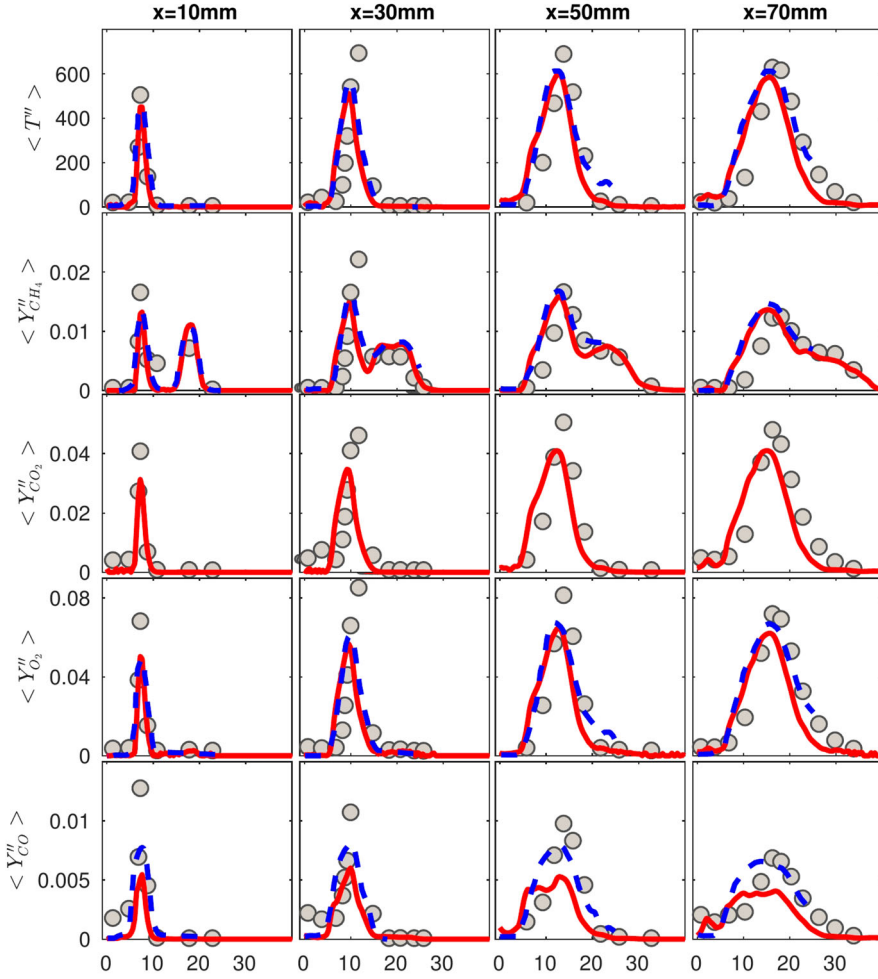

Figure 22. *SwB1*: The radial profiles of the time-averaged rms fluctuating temperature and the rms fluctuating mass fractions of CH_4, CO_2, O_2 and CO at the axial locations of $x = 10, 20, 30, 50$ and $70\,mm$. The symbols: the experimental data; the solid line: the LES/PDF results; the dashed line: the results by Proch and Kempf [40]. (Colour online.)
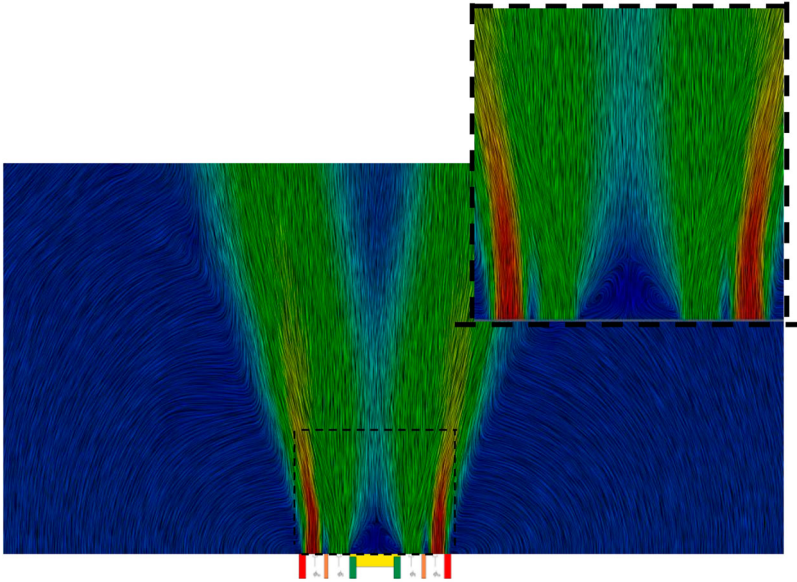
Figure 23. Time-averaged streamlines computed by the present hybrid LES/PDF solver for the *SwB6* case superimposed on the magnitude of the time-averaged resolved axial velocity. (Colour online.)
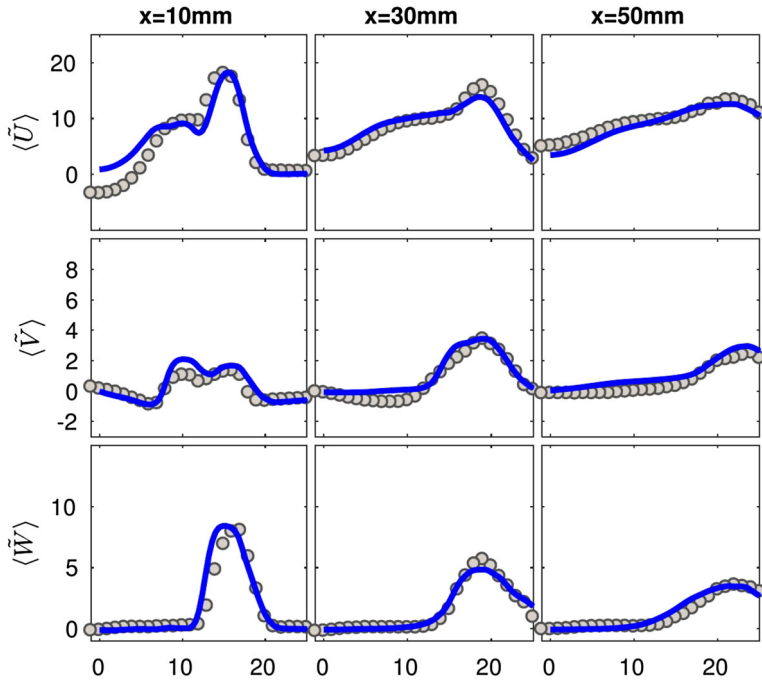

Figure 24. *SwB6*: The radial profiles of time-averaged resolved axial, radial and tangential velocities from top to bottom at axial locations $x = 10$, 30 and 50 mm. The symbols are the experimental data and the solid lines are the LES/PDF results.

are in very good conformity with both the experimental measurements and the previous LES simulations [40].

5.2. *The swirling stratified flame, SwB6*

In this section, the method is applied to simulate the moderately swirling and moderately stratified flame, *SwB6*, and the results are compared with the experimental data [39,46]. First, the time-averaged streamlines are plotted in Figure 23 to show the overall flow pattern for this flame. The flow pattern is qualitatively similar to the experimental flow field but the length of the recirculation zone is predicted around 10 mm that is shorter than the experimental value of 16 mm. This discrepancy is mainly attributed to the extreme sensitivity of the recirculation length to the model parameters. In particular, the length of the
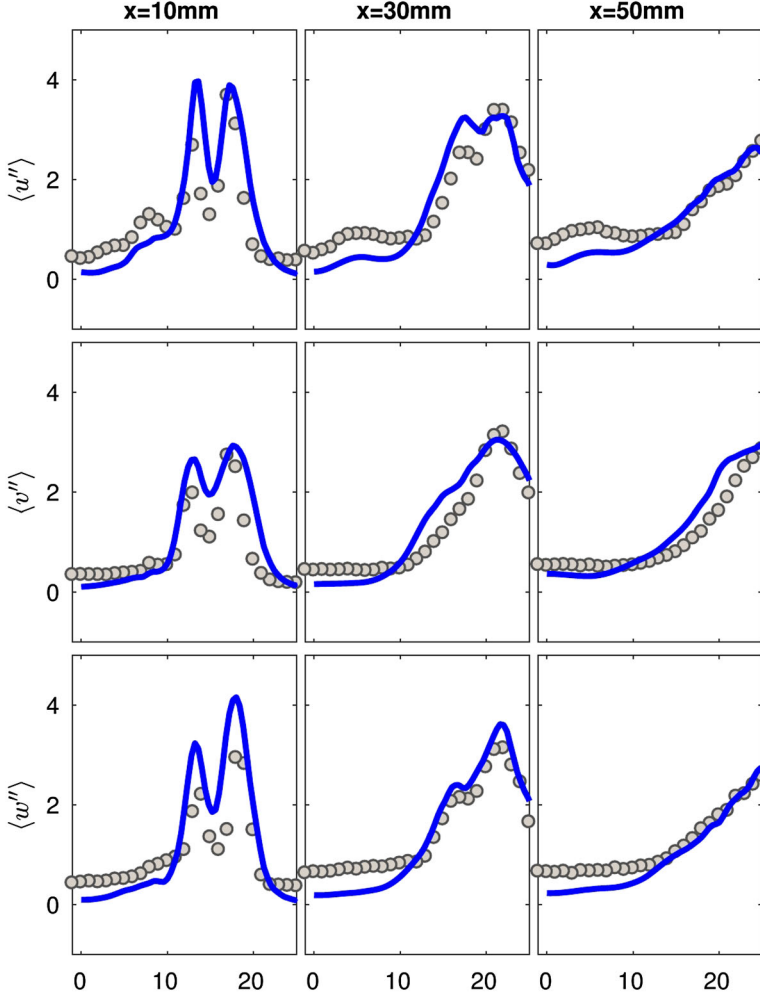

Figure 25. *SwB6*: The radial profiles of the time-averaged rms fluctuating axial, radial and tangential velocities from top to bottom at axial locations $x = 10$, 30 and 50 mm. The symbols are the experimental data and the solid lines are the LES/PDF results.

recirculation zone is found to be very sensitive to the mixing model constant, C_m, which is examined and reported in a companion paper [47]. We next compare the computational results with the experimental data quantitatively. Figure 24 shows the time-averaged radial profiles of the resolved axial $\langle \tilde{U} \rangle$, radial $\langle \tilde{V} \rangle$ and tangential $\langle \tilde{W} \rangle$ velocities at the axial locations $x = 10$, 30 and 50 mm. As seen, the time-averaged velocities are overall in good agreement with the measurements except for the axial velocity at the edge of the recirculation zone, i.e. $x = 10$ mm where the axial velocity is significantly overpredicted. This is consistent with the flow pattern shown in Figure 23 and the results from the underprediction of the recirculation length. Additionally, the axial velocity is slightly underpredicted near the centreline at axial location $x = 50$ mm, which may be attributed to the vortex breakdown occurring in the stratified swirling case, *SwB6*. We note that the vortex breakdown mechanism is very complicated and difficult to resolve computationally due to its sensitivity to the volume expansion rate, and thus to the mixing model constant C_m. A detailed sensitivity analysis of the vortex breakdown is under investigation and will be reported in
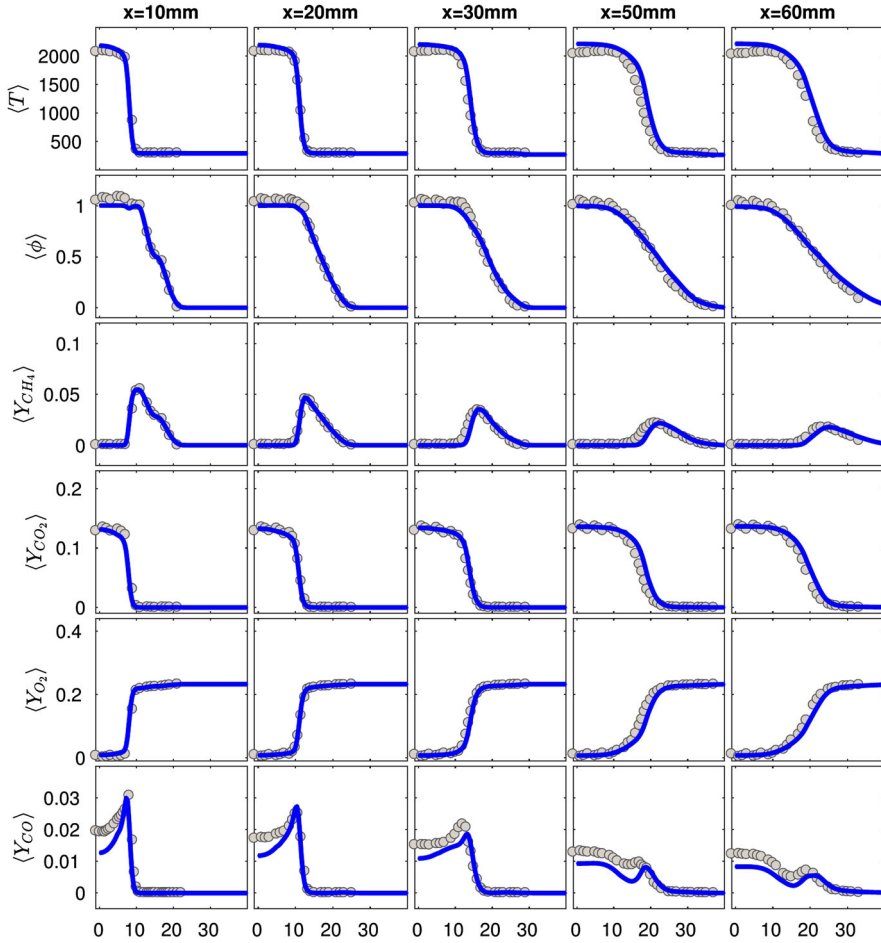

Figure 26. *SwB6*: The radial profiles of the time-averaged resolved temperature and the resolved mass fractions of CH_4, CO_2, O_2 and CO at the axial locations of $x = 10$, 20, 30, 50 and 70 mm. The symbols are the experimental data and the solid lines are the LES/PDF results.

the companion paper [47]. The time-averaged radial profiles of the rms fluctuating axial $\langle u'' \rangle$, radial $\langle v'' \rangle$ and tangential $\langle w'' \rangle$ velocities are shown in Figure 25 at the axial locations $x = 10$, 30 and 50 mm. This figure shows that the rms velocities are consistently underpredicted near the centreline at all axial locations. However, considering the extreme sensitivity and difficulty of resolving the recirculation zone and vortex breakdown, the rms velocities are overall in reasonably good agreement with the experimental results.

The time-averaged radial profiles of the resolved temperature $\langle \tilde{T} \rangle$, the equivalence ratio $\langle \tilde{\varphi} \rangle$ and the mass fractions of CH_4, CO_2, O_2 and CO at the axial locations $x = 10$, 30, 50 and 60 mm are plotted in Figure 26 together with the experimental data. The temperature and the equivalence ratio profiles are overall in good agreement with the experimental data at all the axial locations. However, the temperature profiles are slightly over estimated, while the equivalence ratio profiles are slightly underestimated close to the centreline. Overall the mass fraction profiles are well predicted at all the locations except for that CO is generally underpredicted especially near the centreline. Although this is consistent with the flow field predictions, it may also indicate deficiency of the chemistry model. The
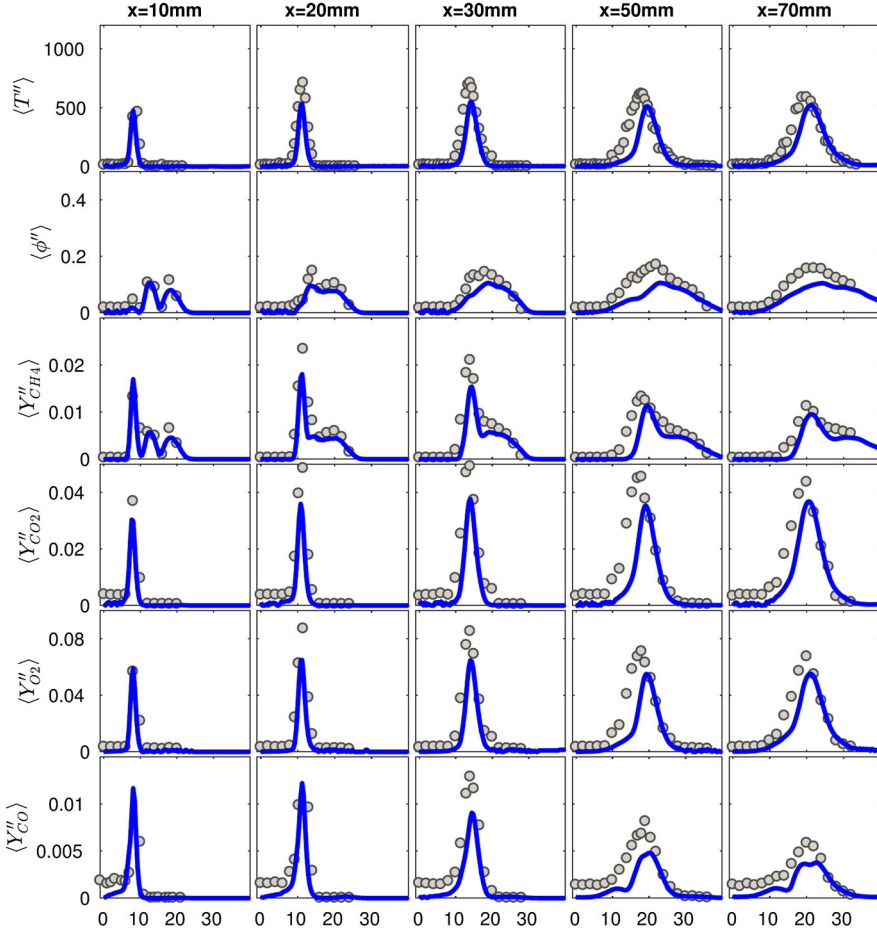

Figure 27. *SwB6*: The radial profiles of the time-averaged rms fluctuating temperature and the rms fluctuating mass fractions of CH_4, CO_2, O_2 and CO at the axial locations of $x = 10$, 20, 30, 50 and 70 mm. The symbols are the experimental data and the solid lines are the LES/PDF results.
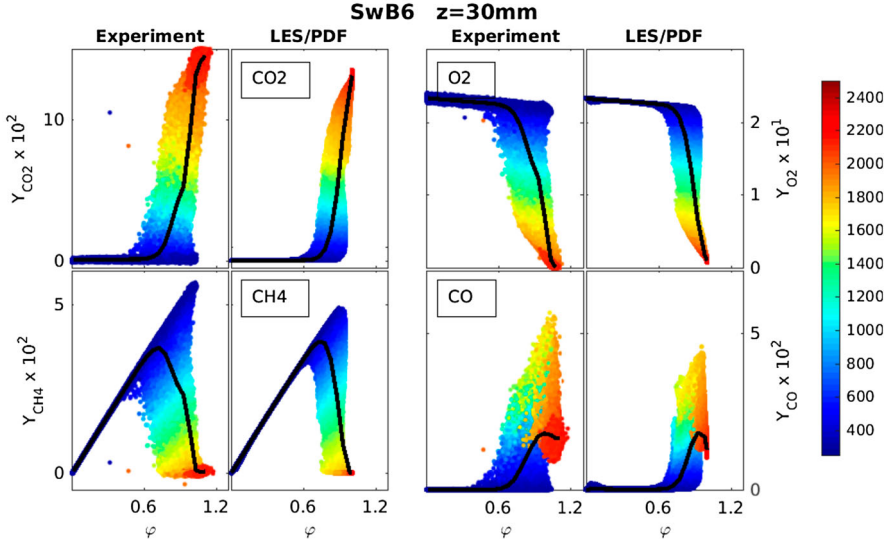
Figure 28. *SwB6*: The scatter plot of mass fractions of CH_4, CO_2, O_2 and CO versus equivalence ratio coded by temperature at the axial locations of $x = 30$ mm. (Colour online.)

time-averaged profiles of the rms fluctuating temperature $\langle T'' \rangle$, the equivalence ratio $\langle \varphi'' \rangle$, and the mass fractions of CH_4, CO_2, O_2 and CO at the axial locations $x = 10$, 30, 50 and 60 mm are shown in Figure 27. Similar to the mean quantities, the rms profiles exhibit a good consistency with the experimental data at all the axial locations except for $\langle Y''_{CO} \rangle$ which is underpredicted especially near the centreline. In addition, all the rms quantities are underpredicted in the downstream locations especially at $x = 50$ mm and $x = 70$ mm, which is mainly attributed to the deterioration of the flow field predictions at these locations.

Finally, the scatter plots of the mass fraction of CH_4, CO_2, O_2 and CO are compared with the experimental data in Figure 28 at axial location $x = 30$ mm. The scatter plots obtained from the LES/PDF simulations are in good agreement with those obtained from the experimental measurements. Furthermore, the mean of the species mass fractions conditional on the equivalence ratio are also in good with the experimental data.

6. Conclusions

An OpenFOAM-based block-structured mesh LES/PDF method is developed for the simulations of turbulent reacting flows in complex geometries. The LES/PDF solver consists of two components: (i) a finite-volume method based LES solver and (ii) a Lagrangian Monte Carlo method based PDF solver. Both components of the hybrid LES/PDF solver are developed entirely within the OpenFOAM framework. The ISAT method developed by Pope [21,22] is incorporated to accelerate the detailed chemical kinetics calculations. The three-stage velocity correction method [11] is also incorporated into the LES/PDF solver for the block-structured grids. The method is fully parallelised using a domain decomposition method.

The accuracy and the numerical consistency of the LES and PDF solvers are examined through the one-way coupling method [15]. For this purpose, simulation of a turbulent piloted methane/air jet diffusion flame (Sandia Flame-D) is performed using a simple

flamelet chemistry model. The fields of the resolved mixture fraction and temperature calculated by the LES and PDF solvers are compared. The results from both solvers are found to be in very good agreement demonstrating consistent coupling of the LES and PDF solvers.

The performance of the three-stage velocity correction method is examined to show the effects of each stage on the numerical accuracy and the consistency of the two solvers. The first-level correction is found to be very efficient in reducing the numerical error and enforcing the consistency between the LES and PDF solvers. Furthermore, the second-level correction is found to be very effective in further eliminating any deviation between the LES and PDF density fields. Additionally, the computational cost required by each stage is also investigated. It is found that the first-level correction increases the computational time consumed by the particle tracking algorithm by only 8%. However, the second-level correction increases the computational cost of the particle tracking by twofold mainly due to the need to solve a linear system of equations that are in the same form as the discrete pressure equation, and use of the Stages 1 and 2 once again to move the particles with the second-level correction velocities.

The Sandia Flame-D simulations are performed using the fully two-way coupled LES/PDF solver with the detailed chemistry representation. The ISAT method is employed in the detailed chemical kinetics calculations. The methane/air combustion is described with an augmented reduced mechanism (ARM1) consisting of 12 steps and 16 species [42]. It is found that the numerical results are in very good agreement with the experimental measurements. The statistical moments of the key chemical species are also predicted quite accurately. The results from the new LES/PDF solver match with the experimental measurements better than those from the previous LES/PDF simulations [43]. The improvement in the numerical results can be attributed to the performance of the particle tracking and the velocity correction methods used in the present PDF solver.

The computational cost of the new LES/PDF solver on block-structured grid is also examined. The PDF component of the LES/PDF solver consumes 85% of the total computational time consumed by the LES/PDF solver. The ratio of the computational cost of the PDF component to the cost of the LES/PDF solver is in the same order of the ratio of the previous PDF solver [7]. This indicates that the new PDF solver on a block-structured grid, and employing the three-stage velocity correction can be computationally as efficient as the PDF solver of Wang and Pope [15] that can accept only a simple structured grid and does not include any velocity correction algorithm.

Finally, the new LES/PDF solver with the detailed chemistry representation is applied to study a turbulent non-swirling premixed flame and a turbulent swirling stratified flame taken from the Cambridge turbulent stratified flame series [24]. The methane/air combustion is described using the ARM1 chemical mechanism. The results are found to be in good agreement with the experimental data. The recirculation zone, and the temperature profiles are predicted accurately at all locations. The present results are also compared with the previous LES simulations that are available only for the non-swirling cases and found to be very consistent.

The present LES/PDF solver has been also used to investigate the effects of the differential diffusion as well as the sensitivity of the results to the mixing model constant C_m for a wider range of the Cambridge turbulent stratified flame series, and the results will be reported in a companion paper [47]. The future work also includes LES/PDF simulations of a dual-swirl gas turbine model combustor (GTMC) studied experimentally by Weigand et al. [48] and Meier et al. [49].

Disclosure statement

Funding

References

[1] S.R. Turns, *An Introduction to Combustion, Concepts and Applications*, Mc Graw Hill, Singapore, 2000.

[2] S.B. Pope, *Turbulent Flows*, Cambridge University Press, Cambridge, 2000.

[3] P.J. Colucci, F.A. Jaberi, P. Givi, and S.B. Pope, *Filtered density function for large eddy simulation of turbulent reacting flows*, Phys. Fluids 10 (1998), pp. 499–515.

[4] V. Raman, H. Pitsch, and R.O. Fox, *Hybrid large-eddy simulation/Lagrangian filtered-density-function approach for simulating turbulent combustion*, Combust. Flame 143 (2005), pp.56–78.

[5] Y. Yang, H. Wang, S.B. Pope, and J.H. Chen, *Large-eddy simulation/probability density function modelling of a non-premixed CO/H$_2$ temporally evolving jet flame*, Proc. Combust. Inst. 34 (2012), pp. 1241–1249.

[6] R. Tirunagari and S.B. Pope, *An investigation of turbulent premixed counterflow flames using large-eddy simulations and probability density function methods*, Combust. Flame 166 (2016), pp. 229–242.

[7] J. Kim and S.B. Pope, *Effects of combined dimension reduction and tabulation on the simulations of a turbulent premixed flame using a large-eddy simulation/probability density function method*, Combust. Theory Model. 18(3) (2014), pp. 388–413.

[8] H. Pitsch, *Large-eddy simulation of turbulent combustion*, Annu. Rev. Fluid. Mech. 38 (2006), pp. 453–482.

[9] F.A. Jaberi, P.J. Colucci, S. James, P. Givi, and S.B. Pope, *Filtered mass density function for large-eddy simulation of turbulent reacting flows*, J. Fluid. Mech. 401 (1999), pp. 85–121.

[10] S.B. Pope, *PDF methods for turbulent reactive flows*, Prog. Energy. Combust. Sci. 11 (1985), pp. 119–192.

[11] Y.Z. Zhang and D.C. Haworth, *A general mass consistency algorithm for hybrid particle/finite-volume PDF methods*, J. Comput. Phys. 194 (2004), pp. 156–193.

[12] M. Muradoglu, P. Jenny, S.B. Pope, and D.A. Caughey, *A consistent hybrid finite-volume/particle method for the PDF equations of turbulent reactive flows*, J. Comput. Phys. 152 (1999), pp. 342–371.

[13] M. Muradoglu, S.B. Pope, and D.A. Caughey, *The hybrid method for the PDF equations of turbulent reactive flows: Consistency conditions and correction algorithms*, J. Comput. Phys. 172 (2001), pp. 841–878.

[14] D.C. Haworth, *Progress in probability density function methods for turbulent reacting flows*, Prog. Energy. Combust. Sci. 36 (2010), pp. 168–259.

[15] H. Wang and S.B. Pope, *Large eddy simulation/probability density function modelling of a turbulent CH$_4$/H$_2$/N$_2$ jet flame*, Proc. Combust. Inst. 33 (2011), pp. 1319–1330.

[16] V. Raman and H. Pitsch, *A consistent LES/filtered-density function formulation for the simulation of turbulent flames with detailed chemistry*, Proc. Combust. Inst. 31 (2007), pp. 1711–1719.

[17] M.R.H. Sheikhi, T.G. Drozda, P. Givi, and S.B. Pope, *Velocity-scalar filtered density function for large eddy simulation of turbulent flows*, Phys. Fluids 15 (2003), pp. 2321–2337.

[18] N. Ansari, G.M. Goldin, M.R.H. Sheikhi, and P. Givi, *Filtered density function simulator on unstructured meshes*, J. Comput. Phys. 230 (2011), pp. 7132–7150.

[19] A. Gupta, *Large-eddy simulation of turbulent flames with radiation heat transfer*, Ph.D. thesis, The Pennsylvania State University, 2011.

[20] OpenFOAM, *The open source CFD toolbox*, OpenFOAM, 2004–2015. Available at http://www.openfoam.com/.

[21] S.B. Pope, *Computationally efficient implementation of combustion chemistry using in situ adaptive tabulation*, Combust. Theory Model. 1 (1997), pp. 41–63.

[22] L. Lu, S.R. Lantz, Z. Ren, and B.S. Pope, *Computationally efficient implementation of combustion chemistry in parallel PDF calculations*, J. Comput. Phys. 228 (2009), pp. 5490–5525.

[23] C. Celis and L.F.F. Silva, *Study of mass consistency LES/FDF techniques for chemically reacting flows*, Combust. Theory Model. 19 (2015), pp. 465–494.

[24] M.S. Sweeney, S. Hochgreb, M.J. Dunn, and R.S. Barlow, *The structure of turbulent stratified and premixed methane/air flames I: Non-swirling flows*, Combust. Flame 159 (2012), pp. 2896–2911.

[25] P. Moin, K. Squires, W. Cabot, and S. Lee, *A dynamic subgridscale model for compressible turbulence and scalar transport*, Phys. Fluids A 3 (1991), pp. 2746–2757.

[26] C. Meneveau, T.S. Lund, and W.H. Cabot, *Lagrangian dynamic subgrid-scale model of turbulence*, J. Comput. Phys. 319 (1996), pp. 353–385.

[27] H. Pitsch and H. Steiner, *Large-eddy simulation of a turbulent piloted methane/air diffusion flame (Sandia Flame D)*, Phys. Fluids 12(10) (2000), pp. 2541–2554.

[28] R. McDermott and S.B. Pope, *A particle formulation for treating differential diffusion in filtered density function methods*, J. Comput. Phys. 226 (2007), pp. 947–993.

[29] J. Villermaux, J.C. Devillon 1972. Representation de la coalescence et de la redispersion des domaines de segregation dans un fluide par un modele d'interaction phenomenologique, in Proceedings of the 2nd International Symposium on Chemical Reaction Engineering, pp. 1–13.

[30] P.P. Popov, H. Wang, and S.B. Pope, *Specific volume coupling and convergence properties in hybrid particle/finite volume algorithms for turbulent reactive flows*, J. Comput. Phys. 294 (2015), pp. 110–126.

[31] P.L. Roe, *Characteristic-based schemes for the Euler equations*, Annu. Rev. Fluid. Mech. 18 (1986), pp. 337–365.

[32] R.I. Issa, *Solution of the implicitly discretised fluid flow equation by operator splitting*, J. Comput. Phys. 62 (1986), pp. 40–65.

[33] J.H. Ferziger and M. Peric, *Computational Methods for Fluid Dynamics*, Springer-Verlag, Berlin, 2002.

[34] R. Cao and S.B. Pope, *Numerical integration of stochastic differential equations: Weak second-order mid-point scheme for application in the composition PDF method*, J. Comput. Phys. 184 (2003), pp. 194–212.

[35] P. Jenny, S.B. Pope, M. Muradoglu, and D.A. Caughey, *A hybrid algorithm for the joint PDF equation for turbulent reactive flows*, J. Comput. Phys. 166 (2001), pp. 281–252.

[36] G.B. Macpherson, N. Nordin, and H.G. Weller, *Particle tracking in unstructured, arbitrary polyhedral meshes for use in CFD and molecular dynamics*, Comm. Numer. Methods Eng. 25 (2009), pp. 263–273.

[37] T.D. Dreeben and S.B. Pope, *Nonparametric estimation of mean fields with application to particle probability density function model for turbulent flows*, Tech. rep., Sibley School of Mechanical and Aerospace Engineering, Cornell University, Ithaca, New York, 1992.

[38] R.S. Barlow and J.H. Frank, *Effects of turbulence on species mass fractions in methane/air jet flames*, Proc. Combust. Inst. 27 (1998), pp. 1087–1095.

[39] M.S. Sweeney, S. Hochgreb, M.J. Dunn, and R.S. Barlow, *The structure of turbulent stratified and premixed methane/air flames II: Swirling flows*, Combust. Flame 159 (2012), pp. 2912–2929.

[40] F. Proch and M. Kempf, *Numerical analysis of the Cambridge stratified flame series using artificial thickened flame LES with tabulated premixed flame chemistry*, Combust. Flame 161 (2014), pp. 2627–2646.

[41] R.R. Tirunagari, M.W.A. Pettit, A.M. Kempf, and S.B. Pope, *A simple approach for specifying velocity inflow boundary conditions in simulations of turbulent opposed-jet flows*, Flow Turbul. Combust. 98 (2017), pp. 131–153.

[42] C.J. Sung, C.K. Law, and J.Y. Chen, *An augmented reduced mechanism for methane oxidation with comprehensive global parametric validation*, Proc. Combust. Inst. 27 (1998), pp. 295–304.

[43] V. Hiremath, S.R. Lantz, H. Wang, and S.B. Pope, *Computationally-efficient and scalable parallel implementation of chemistry in simulations of turbulent combustion*, Combust. Flame 159 (2012), pp. 3096–3109.

[44] J. Janicka, W. Kolbe, and W. Kollman, *Closure of the transport equation for the probability density function of turbulent scalar fields*, J. Non-Equilib. Thermodyn. 4 (1979), pp. 47–66.

[45] G. Esposito and H.K. Chelliah, *Skeletal reaction models based on principal component analysis: Application to ethylene-air ignition, propagation, and extinction phenomena*, Combust. Flame 158 (2011), pp. 477–489.

[46] R. Zhou, S. Balusamy, M.S. Sweeney, R.S. Barlow, and S. Hochgreb, *Flow field measurements of a series of turbulent premixed and stratified methane/air flames*, Combust. Flame 160 (2013), pp. 2017–2028.

[47] H. Turkeri, X. Zhao, B.S. Pope, and M. Muradoglu, *Large eddy simulation/probability density function simulations of Cambridge turbulent stratified flame series with differential diffusion*, Combust. Flame (to be submitted).

[48] P. Weigand, W. Meier, X.R. Duan, W. Stricker, and M. Aigner, *Investigations of swirl flames in a gas turbine model combustor: I. Flow field, structures, temperature, and species distributions*, Combust. Flame 144(1–2) (2006), pp. 205–224.

[49] W. Meier, X.R. Duan, and P. Weigand, *Investigations of swirl flames in a gas turbine model combustor: II. Turbulence–chemistry interactions*, Combust. Flame 144(1–2) (2006), pp. 225–236.